

THE NATURE OF DOUBLE-PEAKED [O III] ACTIVE GALACTIC NUCLEI*

HAI FU¹, LIN YAN², ADAM D. MYERS^{3,6}, ALAN STOCKTON⁴, S. G. DJORGOVSKI^{1,7}, G. ALDERING⁵, AND JEFFREY A. RICH⁴

ApJ accepted 2011 October 24

ABSTRACT

Active galactic nuclei (AGNs) with double-peaked [O III] lines are suspected to be sub-kpc or kpc-scale binary AGNs. However, pure gas kinematics can produce the same double-peaked line profile in spatially integrated spectra. Here we combine integral-field spectroscopy and high-resolution imaging of 42 double-peaked [O III] AGNs from the Sloan Digital Sky Survey to investigate the constituents of the population. We find two binary AGNs where the line-splitting is driven by the orbital motion of the merging nuclei. Such objects account for only $\sim 2\%$ of the double-peaked AGNs. Almost all ($\sim 98\%$) of the double-peaked AGNs were selected because of gas kinematics; and half of those show spatially resolved narrow-line regions that extend 4–20 kpc from the nuclei. Serendipitously, we find two spectrally *unresolved* binary AGNs where gas kinematics produced the double-peaked [O III] lines. The relatively frequent serendipitous discoveries indicate that only $\sim 1\%$ of binary AGNs would appear double-peaked in Sloan spectra and $2.2^{+2.5}_{-0.8}\%$ of all Sloan AGNs are binary AGNs. Therefore, the double-peaked sample does not offer much advantage over any other AGN samples in finding binary AGNs. The binary AGN fraction implies an elevated AGN duty cycle ($8^{+8}_{-3}\%$), suggesting galaxy interactions enhance nuclear accretion. We illustrate that integral-field spectroscopy is crucial for identifying binary AGNs: several objects previously classified as “binary AGNs” with long-slit spectra are most likely single AGNs with extended narrow-line regions. The formation of extended narrow-line regions driven by radiation pressure is also discussed.

Subject headings: galaxies: active — galaxies: formation — galaxies: interactions — galaxies: nuclei — quasars: emission lines

1. INTRODUCTION

The ubiquity of binary supermassive black holes (SMBHs) is expected because of two commonly accepted facts (Begelman et al. 1980): that galaxies frequently merge (Toomre & Toomre 1972) and that SMBHs occupy the centers of the majority of massive galaxies (Kormendy & Richstone 1995; Richstone et al. 1998). If mergers trigger or enhance nuclear accretion as predicted by simulations (Barnes & Hernquist 1996), a significant fraction of mergers should appear as binary active galactic nuclei (AGNs).

Over the last three decades, binary AGNs have been found with separations ranging from parsec to tens of kiloparsec (kpc) scales. Thanks to the Sloan Digital Sky Survey (SDSS), we now have a large sample of binary quasars with separations of tens of kpc; and they account for $\sim 0.1\%$ of the QSO population at $z > 1$ (Djorgovski et al.

1987; Djorgovski 1991; Kochanek et al. 1999; Hennawi et al. 2006; Myers et al. 2007, 2008; Green et al. 2010) and $\sim 3.6\%$ of SDSS spectroscopically selected AGNs between $0.02 < z < 0.16$ (Liu et al. 2011). On kpc-scales, we have six convincing examples, LBQS 0103-2753 (Junkkarinen et al. 2001; Shields et al. 2011), NGC 6240 (Komossa et al. 2003), 3C 294 (Stockton et al. 2004), Mrk 463 (Bianchi et al. 2008), Mrk 739 (Koss et al. 2011), and SDSS J150243.1+111557 (Fu et al. 2011b). On parsec-scales, there is only one convincing example, the radio galaxy 0402+379, for which only the Very Long Baseline Array (VLBA) can resolve the 7-parsec-separation binary (Rodríguez et al. 2006).

Serendipitously discovered binary AGNs are of course interesting objects to study, but in order to understand the effect of galaxy interactions on nuclear activities, it is crucial to estimate the frequency of binary AGNs as a function of physical separation. Systematic searches for parsec-scale binary AGNs have focused on objects with two distinct sets of AGN emission lines, either as double-peaked broad emission lines (Gaskell 1983, 1996; Boroson & Lauer 2009) or as narrow lines offset from the broad lines (Komossa et al. 2008; Eracleous et al. 2011; Tsalmantza et al. 2011). However, double-peaked broad lines are not necessarily binary AGNs—they could be equally well explained as a Keplerian accretion disk (Chen et al. 1989; Eracleous et al. 1997; Eracleous & Halpern 2003). And the narrow-line offset systems could be gravitational wave recoiled black holes (Komossa et al. 2008). Unfortunately, it is difficult to confirm or refute these binary AGN candidates, because of the extremely high spatial resolution needed to resolve the components and/or the long time span needed to monitor the systematic velocity changes due to orbital motion.

The same technique has been used to find binary AGNs with separations larger than the scale of the broad-line regions

* Some of the data presented herein were obtained at the W.M. Keck Observatory, which is operated as a scientific partnership among the California Institute of Technology, the University of California and the National Aeronautics and Space Administration. The Observatory was made possible by the generous financial support of the W.M. Keck Foundation.

¹ Astronomy Department, California Institute of Technology, MS 249-17, Pasadena, CA 91125, USA; fu@astro.caltech.edu

² Spitzer Science Center, California Institute of Technology, MS 220-06, Pasadena, CA 91125, USA

³ Department of Physics and Astronomy, University of Wyoming, Laramie, WY 82071, USA

⁴ Institute for Astronomy, University of Hawaii, 2680 Woodlawn Drive, Honolulu, HI 96822, USA

⁵ Physics Division, Lawrence Berkeley National Laboratory, 1 Cyclotron Road, Berkeley, CA 94720, USA

⁶ Max-Planck-Institut für Astronomie, Königstuhl 17, D-69117 Heidelberg, Germany

⁷ Distinguished Visiting Professor, King Abdulaziz University, Jeddah, Saudi Arabia

but within ~ 10 kpcs. Several systematic searches have compiled AGNs with double-peaked [O III] $\lambda 5007$ emission lines (dpAGNs hereafter) from the DEEP2 survey (Gerke et al. 2007; Comerford et al. 2009) and the SDSS (Xu & Komossa 2009; Wang et al. 2009; Liu et al. 2010b; Smith et al. 2010; Liu et al. 2011). If double-peaked [O III] emission is indicative of a binary AGN, such emission most likely represents objects with transverse separations of ~ 100 parsecs to ~ 10 kpcs (e.g., Wang et al. 2009). However, double-peaked emission lines may also arise from mechanisms other than orbital motion, such as gas kinematics in the narrow-line regions (e.g., Gelderman & Whittle 1994; Fu & Stockton 2009b; Fischer et al. 2011; Shen et al. 2011a), or jet-cloud interactions (e.g., Stockton et al. 2007; Rosario et al. 2010).

Unlike parsec-scale binaries, it is relatively easy to confirm or refute the kpc-scale binary AGN candidates with existing facilities. Shen et al. (2011a) have recently carried out an imaging and long-slit spectroscopic study of 31 SDSS dpAGNs (mostly at declinations of $< 22^\circ$). They identified five binary AGNs, with each resolved galaxy component associated with AGN-photoionized narrow emission lines (i.e., type-2–type-2 pairs). However, their study was limited by the natural seeing and the spatial coverage of the long-slit. To move forward, we decided to carry out a high-resolution imaging and integral-field spectroscopic survey of dpAGNs.

Ground-based imaging aided by adaptive optics enables efficient high-spatial-resolution imaging surveys. In Fu et al. (2011a), we published images of 50 SDSS dpAGNs from the Keck laser guide star adaptive optics system (LGSAO; Wizinowich et al. 2006). With a spatial resolution of $\sim 0.1''$, we found $\sim 30\%$ of dpAGNs at $z < 0.6$ show discernible companions. Using the same instrument, Rosario et al. (2011) found a similar result with a smaller sample. These results showed that at least 70% of the dpAGNs are either single AGNs or binary type-2 AGNs with coalesced host galaxies. It is worth noting that even a merging galaxy associated with a dpAGN could be ascribed to single AGNs—the double-peaked AGN emission lines could arise from a single active component which is merging with a non-active galaxy.

We have extended our LGSAO imaging to a sample doubling the size of that surveyed by Fu et al. (2011a). In addition, we have obtained integral-field spectroscopy of 42 dpAGNs, including most of the merging systems identified with LGSAO imaging. In this paper, we analyze the combined data set to identify kpc-scale binary AGNs and to study the statistics of dpAGN types. We describe our observations in Section 2. In Section 3, we classify the AGNs based on both stellar morphology from high-resolution imaging and ionized gas morphology and kinematics from integral-field spectroscopy. In Section 4 we compare the classifications based on previous long-slit spectroscopy and our integral-field spectroscopy. We show that several objects classified in the literature as “binary” are, most likely, single AGNs with extended narrow-line regions. We conclude by discussing the binary AGN fraction, the efficiency of the double-peaked selection technique, and the formation of extended narrow-line regions (Section 5).

Throughout we adopt a Λ CDM cosmology with $\Omega_m = 0.3$, $\Omega_\Lambda = 0.7$ and $h \equiv H_0/100 \text{ km s}^{-1} \text{ Mpc}^{-1} = 0.7$, consistent with the maximum likelihood estimates from WMAP (Dunkley et al. 2009).

2. OBSERVATIONS

The dpAGNs presented here were selected from the SDSS DR7 spectroscopic data set by several groups (Wang et al. 2009; Liu et al. 2010b; Smith et al. 2010). There are a total of 340 dpAGNs between $0.008 < z < 0.686$, or $\sim 1\%$ of the entire SDSS AGN sample. Their [O III] $\lambda 5007$ lines show double-peaked profiles with velocity splitting ranging from 151 to 1314 km s^{-1} . Initially, it was suspected that most of these double-peaked line profiles could originate from the orbital motions of binary AGNs blended within the $3''$ -diameter apertures of SDSS fibers (e.g., Wang et al. 2009). Nonetheless, to test whether these are binary AGNs, the SDSS data are insufficient because of their limited spatial resolution. To better understand this population of AGNs, we obtained high-resolution ($\sim 0.1''$) adaptive-optics imaging and integral-field spectroscopy for a representative sample of dpAGNs.

2.1. High Resolution Imaging

Six of the dpAGNs have ACS/WFPC2 images in the *HST* archive (SDSS J0807+3900, SDSS J0941+3944, SDSS J1129+5756, SDSS J1301-0058, SDSS J1526+4140⁹ and SDSS J2310-0900). For the rest, we attempted high resolution near-infrared (NIR) imaging with the Keck II laser guide-star adaptive-optics system (LGSAO; Wizinowich et al. 2006). LGSAO observations require a bright ($R \lesssim 18$) star within $\sim 60''$ of the target for tip-tilt corrections. Therefore, we selected 45 type-1 (broad-line) AGNs and 107 type-2 (narrow-line) AGNs that have nearby tip-tilt stars. We further included 23 type-1 AGNs without nearby tip-tilt stars but brighter than $R = 18$ so that the AGN itself could serve as the beacon for tip-tilt corrections. Our final LGSAO target sample contained 173 AGNs over the redshift range $0.023 < z < 0.686$.

We obtained *H*-band (1.473–1.803 μm ; OSIRIS/Hbb filter) images for three sources (SDSS J0400-0652, SDSS J0952+2552, and SDSS J1240+3534) with the OSIRIS imager (Larkin et al. 2006) at $0.02'' \text{ pixel}^{-1}$ on 2010 March 6 and 7 (UT), and *K'*-band (or *K_p*, 1.948–2.299 μm) images for 97 sources on 2010 June 3 and 4 (UT) and 2011 January 5 and 6 (UT) with NIRC2 at $0.04'' \text{ pixel}^{-1}$. For each target, we took at least three 1-minute exposures, dithered within boxes of $4''$ to $7''$ width. For the brightest targets, we used shorter exposure times and a number of co-adds to avoid saturation. The final exposure times and the CFHT/DIMM seeing data are listed in Tables A1 & A2 in the Appendix. Half of our imaging data were presented in Fu et al. (2011a) and we followed the same data reduction procedure here. The astrometry of these images are tied to that of the SDSS using the centroid position of the targets and assuming the pre-determined instrument plate scale.

In summary, we have high-resolution images (FWHM [Full Width Half Maximum] $\sim 0.1''$) for a total of 106 dpAGNs — 37 type-1 and 63 type-2 AGNs were imaged by the Keck II LGSAO in the NIR, and 6 type-2 AGNs were imaged by the *HST* in the optical. Inspecting the images, we found that 31 ($29^{+5}_{-4}\%$)¹⁰ sources have companions within $3''$ (Fig. A1), consistent with the merger fractions found by Fu et al. (2011a) and Rosario et al. (2011).

2.2. Integral-Field Spectroscopy

⁹ SDSS J1526+4140 is also known as NGC 5929

¹⁰ We estimate the 1σ binomial confidence intervals of any fractions from the quantiles of the beta distribution (Cameron 2011).

Integral-field spectroscopy allows us to spatially resolve emission lines—thus comparing emission-line morphologies with continuum morphologies—and to derive the kinematics of the emission lines. Based on this information, we can study the constituents of dpAGNs, as it is known that several mechanisms can produce the same double-peaked line profiles (e.g., Rosario et al. 2010; Fu et al. 2011a; Shen et al. 2011a). The sample that we compiled for integral-field spectroscopy is biased in favor of sources with existing high-resolution imaging data and sources that displayed close companions within $3''$. We obtained seeing-limited optical integral-field spectroscopy for 39 sources and LGSAO-aided integral-field spectroscopy for 3 additional sources. The combined spectroscopic sample includes 26 apparent mergers that show close companions within $3''$, 11 isolated sources, and 5 sources with only seeing-limited images (Table 1). We assume that the 5 sources without high-resolution images are single galaxies.

2.2.1. Adaptive Optics-Aided Integral-Field Spectroscopy

We obtained NIR integral-field spectra with the OH-Suppressing Infrared Imaging Spectrograph (OSIRIS Larkin et al. 2006) on the Keck II telescope for 3 double-peaked AGNs (SDSS J0808+4813, SDSS J1050+0839, and SDSS J1240+3534). OSIRIS was operated with the LGSAO system to deliver high spatial-resolution datacubes.

The OSIRIS observations took place on 2010 March 7 (UT) under excellent conditions. We used the $0.05''$ lenslet scale and either the Kn2 (2.036–2.141 μm) or the Kn3 (2.121–2.229 μm) filter to cover the redshifted Pa α $\lambda 1.87 \mu\text{m}$ line with a $2.25'' \times 3.2''$ (Kn2) or $2.4'' \times 3.2''$ (Kn3) field of view and a spectral resolution $R \simeq 3800$. Three or four on-source exposures of 600 seconds were taken with a 600-second sky frame in between. An A1V star, HIP 49198, was observed for telluric absorption correction and flux calibration.

We reduced the data using the OSIRIS data reduction pipeline (version 2.3; Krabbe et al. 2004). In summary, the pipeline subtracts darks and biases from the raw images, removes crosstalk signals, identifies glitches, cleans cosmic-rays, extracts and wavelength-calibrates spectra from individual lenslets, assembles the datacubes, corrects for differential atmospheric refraction, subtracts sky using an implementation of the scaled sky subtraction algorithm (Davies 2007), removes telluric absorption, and co-adds the individual exposures to form the final datacube. The spatial resolution of the final datacubes is $\sim 0.12''$.

2.2.2. Seeing-Limited Integral-Field Spectroscopy

We obtained seeing-limited integral-field spectra using the Supernova Integral-Field Spectrograph (SNIFS; Aldering et al. 2002; Lantz et al. 2004) on the University of Hawaii 2.2-meter telescope (Mauna Kea) in a fully remote observing mode. SNIFS is a pure-lenslet integral-field spectrograph similar to TIGER (Bacon et al. 1995). It has a fully filled $6.45'' \times 6.45''$ field of view sampled by a 15×15 grid of $0.43'' \times 0.43''$ spatial elements. The dual-channel spectrograph covers wavelengths from 3200 to 10000 \AA simultaneously with a spectral resolution of $\text{FWHM} = 6.1$ and 8.2\AA for the blue (3200–6000 \AA ; $R \sim 700$) and red (5000–10000 \AA ; $R \sim 1000$) spectrographs, respectively. The instrument position angles (PAs) are fixed on the sky — $2.6 \pm 0.8^\circ$ for the blue and $5.0 \pm 1.2^\circ$ for the red. We measured the spectral resolution from arc lamp exposures taken with each science

exposure and they agree well with the measurements from the night sky lines in the final reduced datacubes.

Our SNIFS observations took place on the first half-nights of 2010 August 4, 6, 8, 9 and on the two full nights of 2011 March 26, 29 (UT). In addition, a 15-minute exposure of SDSS J1155+1507 was taken on 2010 November 21 (UT). The 2010 run was photometric with seeing between $0.6''$ and $1.2''$, and the 2011 run was cloudy with seeing between $0.8''$ and $2''$. Depending on the [O III] $\lambda 5007$ line fluxes and the observing conditions, the total integration time ranged from 10 to 60 minutes for each object. Table 1 presents the observing log.

The raw data were first passed through the SNIFS data reduction pipeline (Aldering et al. 2006). After subtraction of biases and a diffuse-light component, the pipeline extracted the spectra from the CCD and reassembled them into (x, y, λ) -datacubes, which were subsequently wavelength calibrated, flat-fielded, and cosmic-ray cleaned. Then, we used our custom IDL scripts to subtract the sky using regions free of object light, to rectify the field to PA = 0, to correct for differential atmospheric refraction as computed by the SLA_REFRO routine in the SLALIB library¹¹ (version 2.5-4), and to join the blue and red channel datacubes. For flux calibration, we used the SDSS spectra. We used standard star observations exposed on the same nights as the data frames to remove telluric absorption features. Finally, Galactic extinction was removed using the dust map of Schlegel et al. (1998) and the standard reddening curve of Cardelli et al. (1989) with $R_V = 3.1$. Considering only spectra with [O III] $\lambda 5007$ peak-to-noise ratio greater than 2.0 as valid, we reached a surface brightness depth of $1.4 \pm 1.0 \times 10^{-16} \text{ erg s}^{-1} \text{ cm}^{-2} \text{ arcsec}^{-2}$ (Table 1 Column 6). The depth varies with exposure time, observed wavelength, and atmosphere conditions. But for all of the sources, our datacubes are sensitive enough to detect both [O III] components seen in the SDSS spectra with at least five spatial elements, assuming the surface brightness profile of the components follows a Gaussian distribution with FWHM less than $2''$. We also confirm that SNIFS detects both [O III] components by comparing the [O III] line profiles extracted from the datacubes with those from SDSS smoothed to SNIFS resolution.

We spatially register the datacubes with the high-resolution images by measuring the centroid position of the target from emission-line-free continuum images stacked from the datacubes. When there are multiple components, we use the centroid of the brightest component. For unresolved sources, the centroid accuracy is approximately equal to FWHM/SNR (signal-noise-ratio). The stacked continuum images from the SNIFS datacube have rather high SNR, so the centroids can be pinned down better than $0.05''$ given the typical resolution of $\text{FWHM} = 1.0''$, despite that the pixel size is $0.4''$. The centroids from the Keck and *HST* images can be measured more accurately than the SNIFS images.

The instrument PA and plate scale previously determined by the SNIFS instrument team are verified by comparing the observed differential atmospheric refraction from standard stars with that predicted by SLA_REFRO using the observed atmosphere conditions.

3. CLASSIFICATION

Broadly speaking, the double-peaked [O III] line profiles could arise from: (1) the orbital motion of a binary AGN, (2)

¹¹ <http://star-www.rl.ac.uk/star/docs/sun67.htx/sun67.html>

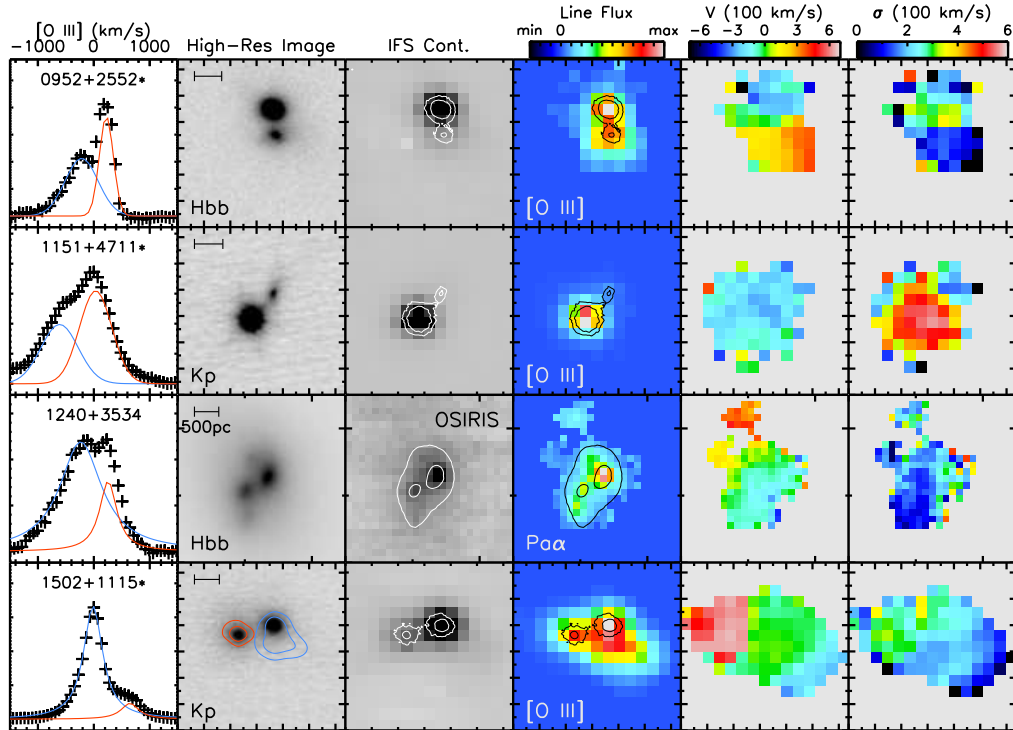


FIG. 1.— Binary AGNs. For each object, from left to right are: the SDSS [O III] $\lambda 5007$ line profile, the highest-resolution broad-band image, the emission-line-free continuum from the datacube, the emission-line intensity map, the velocity map, and the velocity dispersion map. Object designations are labeled in the first column and broad-line AGNs are indicated with stars. The two-component fit to the [O III] line profile is overplotted. The filter for the broad-band images are labeled, and the scale bar indicates a transverse separation of 5 kpc, unless otherwise indicated. For objects where SNIFS spectrally resolves the kinematic components, we overlay the emission-line fluxes from the blueshifted and redshifted components as blue and red contours on the broad-band image. Contours in third and fourth columns are from the broad-band images in the second column, which have been spatially aligned with the datacubes. The emission line that we measured are labeled in the fourth column. In all of the images, N is up and E is to the left; major tickmarks are spaced in $1''$. Note that the maps of SDSS J1240+3534 are from OSIRIS.

gas kinematics in extended narrow-line regions (ENLRs), and (3) unresolved nuclear gas kinematics (e.g., aligned outflows or disk rotation on small scales). We classified the 42 IFS-observed dpAGNs into these three broad categories by examining the continuum and emission-line morphologies and the kinematics of the ionized gas. We emphasize that we obtained $\lesssim 0.1''$ resolution images (§ 2.1) for 37 of the 42 IFS-observed sources.

We derived maps of emission-line fluxes and kinematics by fitting Gaussians at each spatial element of the datacube. These maps are shown in Figures 1, 4, & 5 along with the best-available broad-band images. If SNIFS spectrally resolves the double-peaked emission lines, we fit two Gaussians with relative velocities fixed to that determined from the Sloan spectra. In the kinematic maps, we show only the brighter component at each position; but in the line flux maps, we use the total flux. For the OSIRIS data, we fit only single Gaussians because OSIRIS spatially resolved the kinematic components.

Table 2 summarizes the basic properties of the sample, grouped by our best-effort classification. The reality is, however, much more complicated than this single-parameter classification because of the following facts:

(1) Each object may contain more than two emission-line components. For example, in SDSS J1440+6156 the two major kinematic components originate from an unresolved nuclear region, but we clearly detected [O III] emission extending $\sim 2''$ to the north of the nucleus. Our first-order classification is based on the main mechanism that produced the double-peaked [O III] line in the Sloan spectra, but we note the second-order mechanisms in Column 11 of Table 2.

(2) SNIFS data have lower spatial resolution than that of the AO/*HST* images. The seeing-limited SNIFS data cannot spatially resolve structures on scales smaller than $\sim 1.2''$. But seven of our SNIFS-observed sources show multiple components within $1.2''$. Except for SDSS J0952+2552, which is a clear binary AGN (Fig. 1), they are all difficult to classify. For example, in SDSS J1108+0659 the merging galaxies seen in the high-resolution images are completely enshrouded by the ENLR. Although it is clear that the ENLR produces the double-peaked line profile, it remains ambiguous whether both of the merging galaxies host AGNs or a single AGN is powering the ENLR. Decomposing the velocity components helps the classification, because the flux centroids of each decomposed component can be localized much more accurately than the seeing disk (to $\sim \text{FWHM}/\text{SNR}$). But it is impossible to rule out the existence of emission-line regions that spatially coincide with the nuclei. Classifications are thus ambiguous for these six compact mergers. On the other hand, spectral decomposition can only be done for sources where SNIFS resolves the line profiles, which leads us to our third caveat...

(3) ... SNIFS data have lower spectral resolution than that of the SDSS spectra, so it can only spectrally resolve the double-peaked emission-lines when the velocity splitting is sufficiently large and/or the components are sufficiently narrow.

Bearing these caveats in mind, in the following subsections we describe the three classes of dpAGNs in detail.

3.1. Binary AGNs

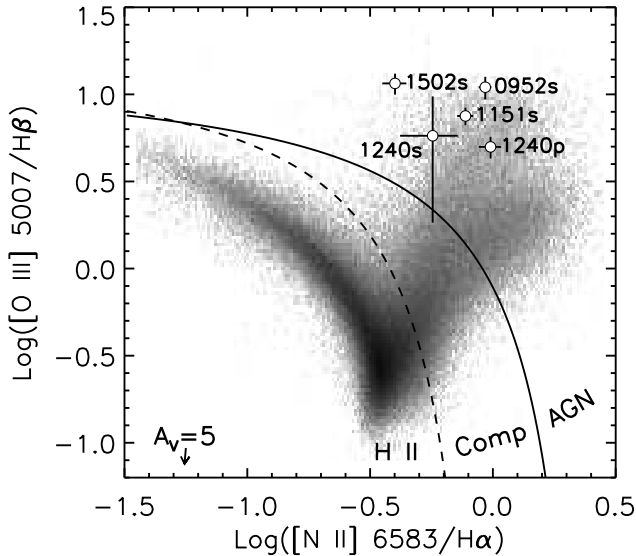


FIG. 2.— BPT diagnostic diagram. The line ratios of the narrow-line components in the binary AGNs indicate AGN photoionization. Our measurements are shown as circles with 1σ error bars. For SDSS J0952+2552, SDSS J1151+4711, and SDSS J1502+1115, we only show line ratios of the secondaries (“s”) because their primaries (“p”) are broad-line AGNs. The background image shows the density distribution of the SDSS emission-line galaxies in log scale. Objects above the solid curve are dominated by AGNs (LINERs are concentrated in the lower denser branch and Seyferts in the upper branch; Kewley et al. 2006), below the dashed curve are star-forming galaxies (Kauffmann et al. 2003), and AGN/star-forming composite galaxies are in between. The arrow shows a reddening vector for a V-band extinction of 5 magnitudes.

We found four binary AGNs; these are merging galaxy pairs where the stellar nuclei spatially coincide with distinctive [O III] emission-line components (Figure 1). However, there are only two systems, SDSS J0952+2552 and SDSS 1502+1115, whose double-peaked [O III] lines are produced by the relative velocities of the merging galaxies. SDSS J0952+2552 was also identified as a binary AGN by OSIRIS (McGurk et al. 2011). The other two are serendipitous binaries, where “serendipity” means that the binaries cannot be resolved in velocity space with a spatially integrated spectrum. SDSS 1240+3534 is double-peaked because of a high-velocity nebula that is spatially offset from the nuclei. The projected separation of the nuclei is only 500 pc. In SDSS 1151+4711, the spectrally resolved emission-line components are spatially unresolved. Hence, we grouped the last two systems under “Extended Narrow-Line Region (ENLR)” and “Unresolved” in Table 2. We note that the emission lines from the NW companion of SDSS 1151+4711 are *not* scattered light from the primary because they are much narrower.

The primaries¹² of three of the four systems are broad-line AGNs (SDSS J0952+2552, SDSS J1151+4711, and SDSS J1502+1115). To test whether their companions are also AGNs, we extracted spectra at the companion locations with $0.85''$ apertures from the SNIFS datacubes. In all three cases, only narrow lines are seen, and their [O III]/H β and [N II]/H α ratios place them securely in the Seyfert regime on the classic “BPT” (Baldwin et al. 1981) line-ratio diagnostic diagram (Fig. 2). Therefore, these are type-1–type-2 binaries.

For the narrow-line AGN SDSS J1240+3534, the Pa α line

¹² We define the primaries as the brighter nucleus in the broad-band images.

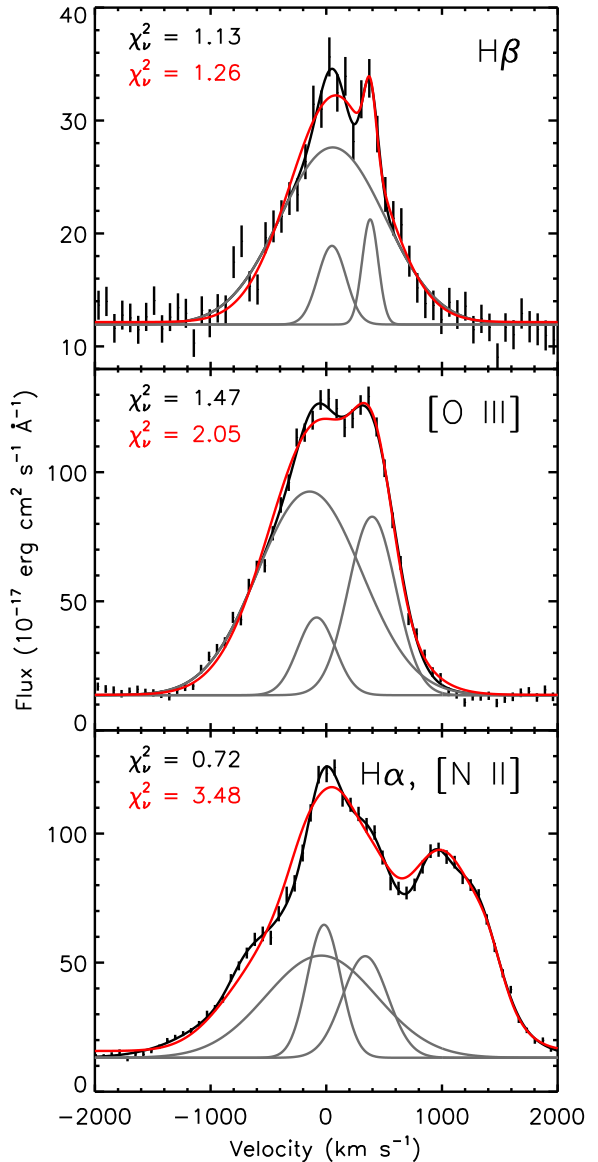


FIG. 3.— Decomposing the emission lines of SDSS J1240+3534. The SDSS spectrum are black data points with error bars. The best-fit components from the three-Gaussian models are in grey, and the sum of the components are in black. The broad and narrow blueshifted components are from the primary and secondary nucleus, respectively, and the redshifted component is from the nebula 0.6 NNE of the nuclei (Fig. 1). The best-fit two-Gaussian models are the red curves. The reduced χ^2 values are labeled for the three-Gaussian model and two-Gaussian model in black and red, respectively.

is spatially resolved into three major components by OSIRIS (two associated with the nuclei, one offset to the NNE). The velocity map implies that the emission-line components at the two stellar nuclei have very similar line-of-sight velocities. To place them on the BPT diagram, we decompose each of the emission lines by fitting three Gaussians simultaneously with MPFIT (Markwardt 2009). We set their initial velocities at those determined from the OSIRIS datacube but allow them to vary during the fit. Figure 3 shows the result. The three-Gaussian models provide better fits to the SDSS line profiles than two-Gaussian models, with the χ^2 values reduced by 10%, 30% and 80% for H β , [O III] λ 5007 and the

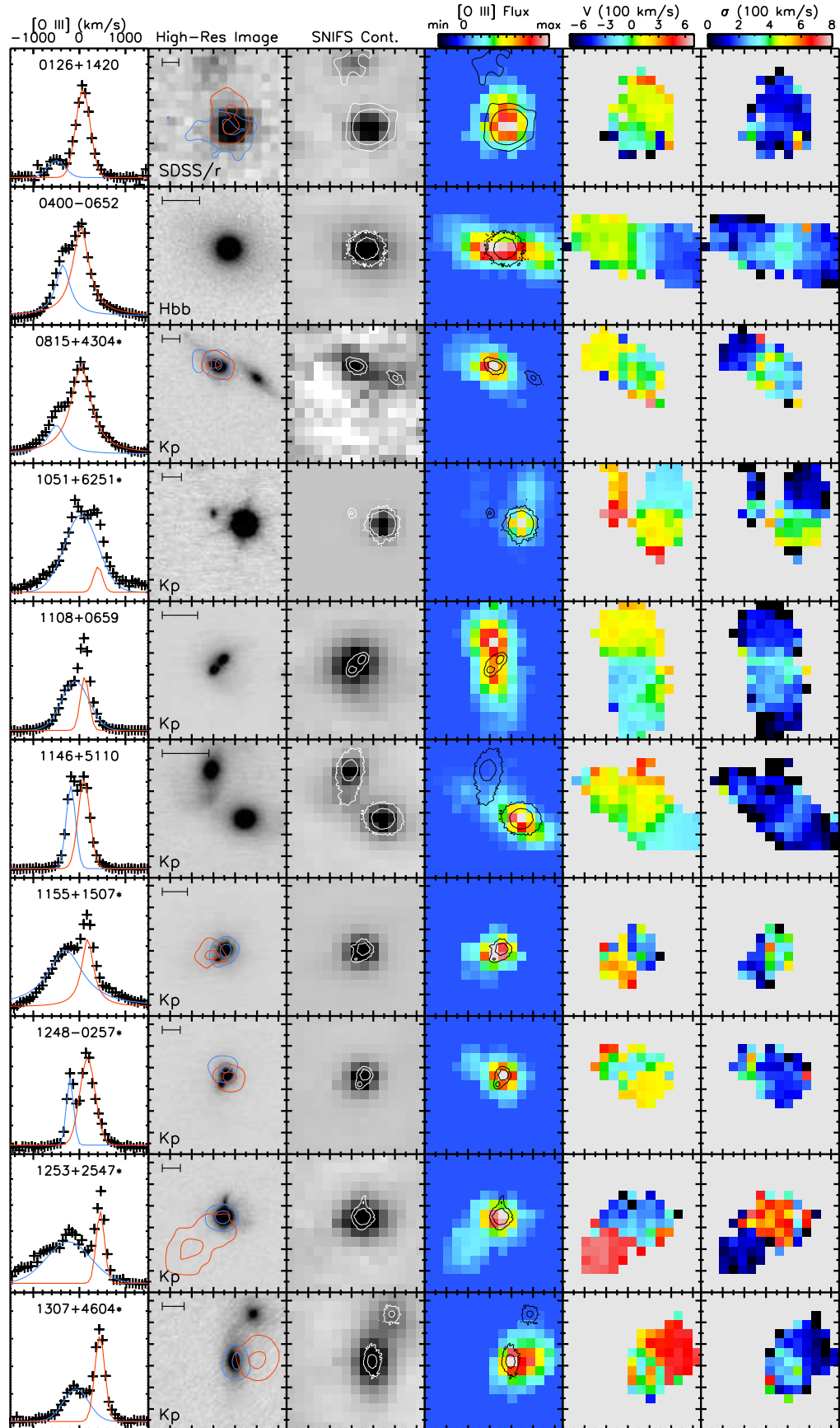


FIG. 4.— Same as Fig. 1 but for dpAGNs where extended narrow-line regions produced the double-peaked [O III] lines. See Fig. 1 for SDSS J1240+3534.

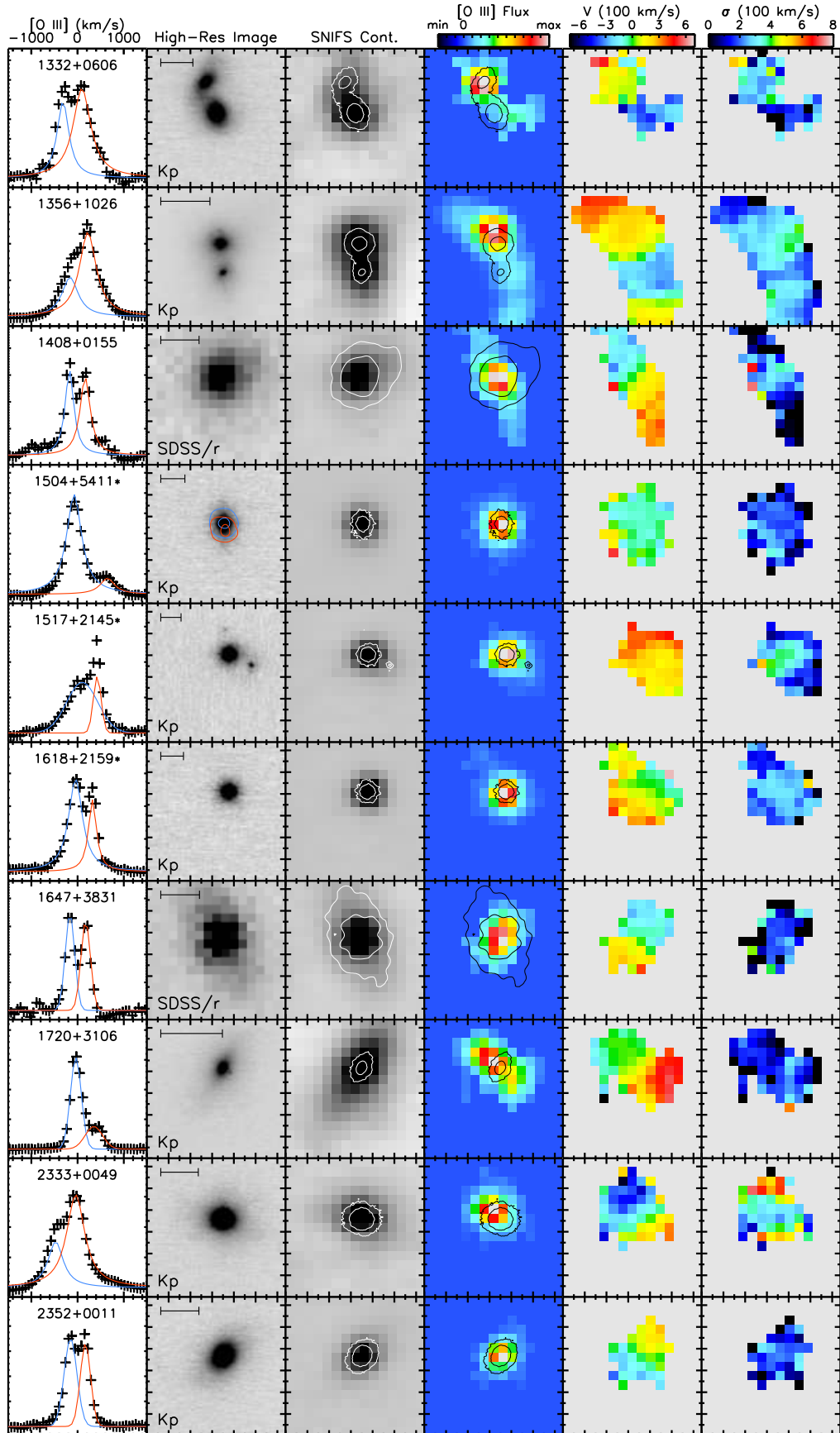


FIG. 4.— *continued.*

[N II]–H α complex, respectively. The 1σ errors of the parameters were computed from the covariance matrix by MPFIT. The decomposed line ratios of the two nuclear components are consistent with AGN photoionization (Fig. 2), indicating that SDSS J1240+3534 is a type-2–type-2 binary.

It should be emphasized that the proof that the gas is photoionized by an AGN does not imply that there is an AGN at the location of the nebula. Because of the proximity between the nuclei in all of these systems, it remains ambiguous whether there is one or two ionizing sources (i.e., AGNs) in each system without high-resolution X-ray or radio images. Recently, the binary nature of SDSS J1502+1115 was confirmed by high-resolution radio continuum images from the Expanded Very Large Array (EVLA) (Fu et al. 2011b).

3.2. Extended Narrow-Line Regions

Our IFS data spatially resolved the emission-line nebulae in half (21/42) of the dpAGNs. We refer to such less luminous nebulosity on kpc scales as ENLRs and reserve the term *Extended Emission-Line Region* (EELR) for luminous nebulae on tens of kpc scales (Stockton & MacKenty 1987; Fu & Stockton 2009a). Nonetheless, four of our ENLR objects (SDSS J0126+1420, 0815+4304, 1051+6251, and 1253+2547) have extended [O III] luminosity greater than 5×10^{41} erg s $^{-1}$ at radii greater than 10 kpc, satisfying the definition of EELRs. We consider an emission-line region extended if the offset between the [O III] centroid and the closest stellar nucleus is greater than $\sim 0.4''$. It is interesting that ENLRs are *equally* represented in merging (13/26) and isolated (8/16) dpAGNs.

SDSS J1240+3534 was observed by OSIRIS, so the datacube has much better spatial resolution. Although SDSS J1240+3534 is a binary AGN (§ 3.1), we include it here—in the ENLR category—because the ENLR produced the redshifted emission line and SNIFS would have resolved the two major spectral components ($\Delta\theta \sim 0.6''$) through spectral decomposition.

Six of the 21 ENLR sources have a secondary classification of “ambiguous”. These sources show resolved stellar components within $1.2''$, and the seeing-limited spatially extended [O III] emission envelops the stellar components. Therefore, we classified them as “ambiguous” because they could still be binary AGNs (Caveat #2 at the beginning of the section).

3.3. Unresolved Narrow-Line Regions: Aligned or Young Outflows?

Finally we consider the category of unresolved narrow-line regions. For the 19 sources in this last category, the centroids of the two major spectral components of each source spatially overlap (Fig. 5). It is possible that these sources can be spatially resolved by AO-aided integral-field spectroscopy with OSIRIS. But it is clear that a fraction of dpAGNs will remain unresolved even at $0.1''$ resolution, as seen in the example of SDSS J1050+0839. OSIRIS *did*, in fact, spatially resolve the gas kinematics in the nuclear NLR of SDSS J0808+4813. For consistency, we include SDSS J0808+4813 in the unresolved category because the spectral components are separated by less than $\sim 0.2''$, so it would not have been resolved by SNIFS. Although the velocity gradient appears along the major axis of the host galaxy, SDSS J0808+4813 is unlikely a nuclear disk: because the K -band luminosity indicates a total stellar mass of $\sim 2 \times 10^{10} M_{\odot}$, the virial mass within the central 200 pc ($V^2 R/G = 1.8 \times 10^9 (V/200 \text{ km s}^{-1})^2 (R/200 \text{ pc}) M_{\odot}$) seems

too large to be gravitationally confined. We believe most of these spatially unresolved dpAGNs are aligned or young outflows.

Among the 11 merging galaxies in this category, SDSS J1151+4711 is a binary AGN (§ 3.1), SDSS J0924+0510 is ambiguous ($\Delta\theta = 0.4''$), SDSS J1239+5314 has an ENLR, and the rest appear to be single AGNs. Of course, we cannot exclude faint [O III] emission from the companions below our SNIFS sensitivity limit ($\simeq 1.4 \pm 1.0 \times 10^{-16}$ erg s $^{-1}$ cm $^{-2}$ arcsec $^{-2}$; § 2.2.2) or AGNs without optical signatures.

4. INTEGRAL-FIELD VS. LONG-SLIT SPECTROSCOPY

Six of the 42 IFS-observed sources overlap with the long-slit sample of Liu et al. (2010a) and Shen et al. (2011a). The overlapped sample includes 4 binary AGNs, 1 resolved NLR (similar to our “ENLR” class), and 1 ambiguous source (similar to our “unresolved” class) according to their classification. These sources are noted in Table 2 and are all in our ENLR category (Fig. 4). Our classifications differ from theirs for the same sources because of the complete spatial coverage of the IFS data. This result highlights the importance of integral-field spectroscopy in classifying dpAGNs. In the following, we discuss the overlapping sources in details.

We agree on the classification of SDSS J0400–0652 as an ENLR source. Shen et al. (2011a) showed two long-slit spectra at PA = 95° and 173° ; and only the spectrum at PA = 95° shows the ENLR, in agreement with the gas morphology we see in the SNIFS datacube (Fig. 4).

We classified SDSS J1108+0659 as an ambiguous ENLR source because the two nuclei, separated by $0.7''$, are swamped by the much larger ($\sim 4''$) ENLR. Liu et al. (2010a) measure only a $0.9''$ separation between the [O III] components in their long-slit spectrum because the slit is aligned with the nuclei, and therefore, it missed the bulk of the emission from the ENLR.

Our IFS data suggest that the other three of the four supposed binary AGNs in their sample are likely ENLRs powered by single AGNs (SDSS J1146+5110, SDSS J1332+0606, and SDSS J1356+1026), although additional data are required to test both scenarios. For SDSS J1146+5110, the NE nucleus shows strong H α emission but non-detectable [O III] emission, so the gas is likely photoionized, at least partly, by star formation. The 2D spectrum of Liu et al. (2010a) shows clearly three kinematic components in [O II], H α , and [N II] but only two prominent SW components in [O III]. The authors classified SDSS J1332+0606 and SDSS J1356+1026 as binary AGNs because the emission-line clouds in the ENLRs are aligned at similar PAs to the stellar components. Note that for both SDSS J1332+0606 and SDSS J1356+1026, the centroids of the [O III] emission are offset from the southern nuclei by a few kpcs and the emission seen at the locations of these nuclei are likely due to seeing smearing. Of course, we cannot rule out the possibility that the observed offset is due to blending between a weak nuclear NLR and a strong offset emission-line nebula, like in the case of SDSS J2333+0049 (Fig. 4). Future deep IFS data with higher spatial resolution can test this scenario.

Shen et al. (2011a) did not spatially resolve the ENLR of SDSS J2333+0049 because their long-slit PA of 117° is almost perpendicular to the elongated orientation of the ENLR.

5. DISCUSSION

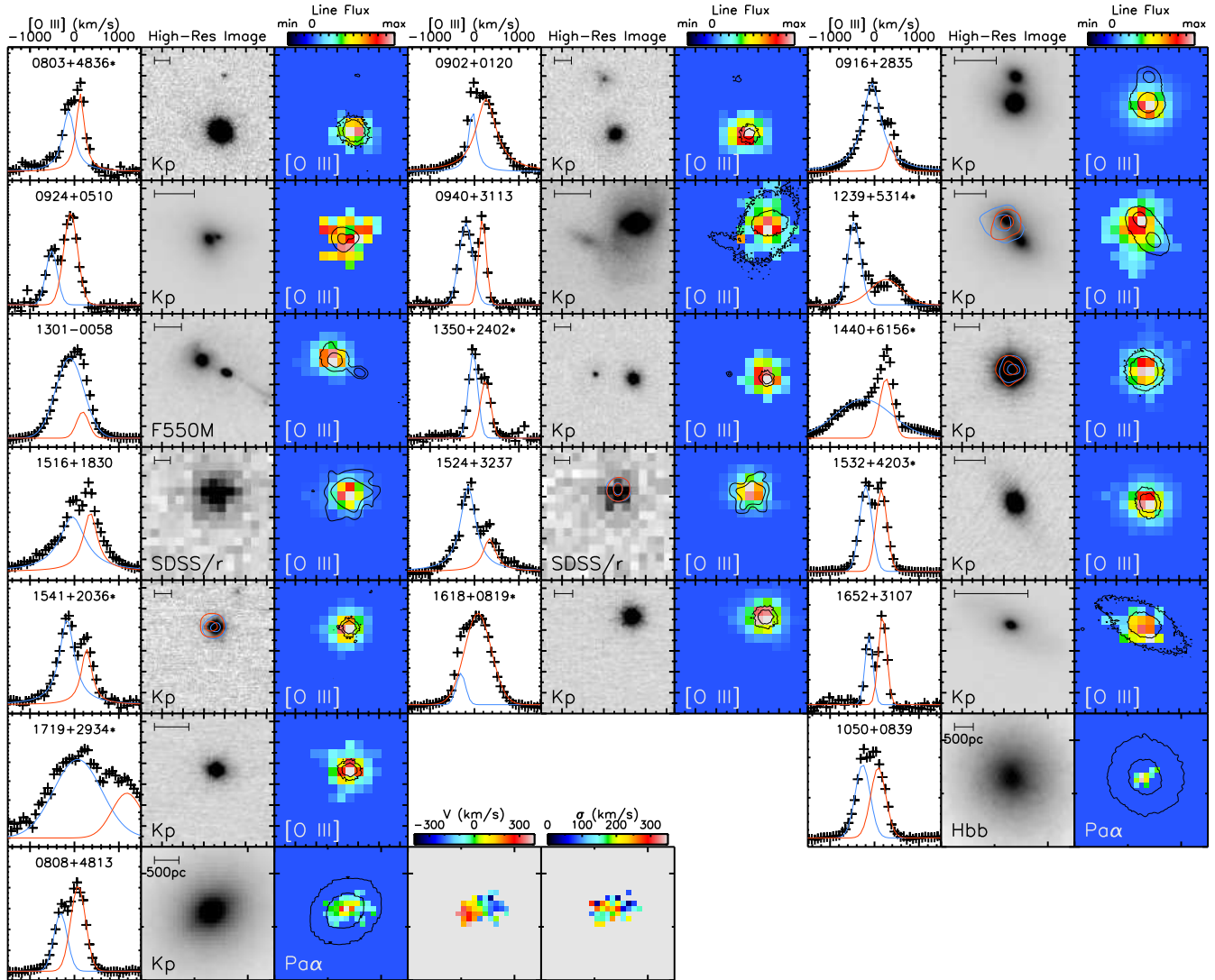


FIG. 5.— Double-peaked AGNs with spatially unresolved kinematics. See Fig. 1 for SDSS J1151+4711. For each source, we show the [O III] λ 5007 velocity profile from the SDSS, the best-available broad-band image, and the emission line flux map from the IFS datacube. N is up and E is left in all images. Like in Fig. 1, for objects where SNIFS spectrally resolves the kinematic components, we overlay the emission-line fluxes from the blueshifted and redshifted components as blue and red contours in the broad-band images. Note that the K_p image of SDSS J1652+3107 does not show the companion clearly; see the contours in the associated line flux map for the position of the faint companion. The IFS data of SDSS J0808+4813 and SDSS J1050+0839 are from OSIRIS, so they are shown in last two rows. For SDSS J0808+4813, we also show the $P\alpha$ kinematic maps because it is resolved at $0.1''$ resolution.

5.1. Statistics of Double-Peaked AGN Types

The majority of dpAGNs are due either to ENLRs or to small-scale gas kinematics. ENLRs account for half (21/42) of our IFS-observed dpAGNs in both merging (13/26) and isolated sources (8/16). We thus expect ENLRs around 50% of dpAGNs. Unresolved gas kinematics account for 45% (19/42) of the IFS-observed dpAGNs, which splits into 42% (11/26) and 50% (8/16) in merging and isolated AGNs, respectively. Taking into account the bias of the IFS sample, we expect 48% of dpAGNs are due to unresolved nuclear gas kinematics.

We found four promising binary AGNs. Only two of these have a double-peaked line profile attributable to the relative velocity difference of the merging nuclei; for the other two the double-peaked profile is a result of gas kinematics. Binary AGNs thus account for 15% (4/26) of the merging dpAGNs (that we have *resolved*). There are seven ambiguous cases for which we cannot rule out the binary AGN scenario, be-

cause of the limited spatial resolution of the SNIFS datacubes (Table 2). If we assume that all of the ambiguous cases are binaries, then we get an upper limit of 42% (11/26) for the binary AGN fraction in merging dpAGNs.

From our high-resolution imaging survey we found that only 29% (31/106) of dpAGNs are mergers; and for the purpose of this discussion, let us assume that AGNs with a single stellar nucleus cannot be kpc-scale binary AGNs. Therefore, we conclude that the binary AGN fraction in dpAGNs is 4.5–12%¹³. If we include the ambiguous cases, our result agrees with that of Shen et al. (2011a) (\sim 10%), although we have identified a different set of binary AGNs (see § 4). In the next subsection, we discuss the binary AGN fraction in all SDSS AGNs.

¹³ The total percentage of the above three categories exceeds 100% because 2–9 of the binary AGNs also belong to the other two categories.

5.2. Binary AGN Fraction and Completeness of Double-Peaked Selection

From a Monte Carlo simulation assuming identical intrinsic relative velocities (500 km s^{-1}) and line widths (250 km s^{-1}) for all systems, Shen et al. (2011a) estimated that roughly 20% of kpc-scale binary AGNs would have been selected as a double-peaked AGN from SDSS fiber spectra. In the following, we attempt to constrain the total binary fraction of all SDSS AGNs (f_{Bin}) and the completeness of the double-peaked selection to kpc-scale binaries (c_{dp}) using the four promising binary AGNs we have identified in a sample of 26 merging dpAGNs.

Because $\sim 1\%$ of AGNs are double-peaked (f_{dp} ; Wang et al. 2009; Liu et al. 2010b; Smith et al. 2010) and $29^{+3}_{-4}\%$ of dpAGNs are resolved mergers in our $0.1''$ -resolution images, the fraction of AGNs that are binaries where orbital motion has produced the line-splitting is $0.022^{+0.025}_{-0.008}\%$ ($2/26 \times 29\% \times 1\%$; errors have been propagated); and it should be the product of the total binary fraction and the double-peaked selection completeness:

$$f_{\text{dpBin}} = f_{\text{Bin}} c_{\text{dp}} \quad (1)$$

Similarly, the fraction of serendipitous binaries among AGNs where other mechanisms produced line splitting is $0.022^{+0.025}_{-0.008}\%$ ($2/24 \times 24/26 \times 29\% \times 1\%$). Assuming that binary AGN do not tend to drive physical mechanisms (such as outflows) that can produce double-peaked emission lines, the serendipitous binary fraction should be the product of the kinematic dpAGN¹⁴ fraction in all AGNs, the total binary fraction, and the double-peaked selection incompleteness ($1 - c_{\text{dp}}$):

$$f_{\text{seBin}} \simeq f_{\text{dp}} f_{\text{Bin}} (1 - c_{\text{dp}}) \quad (2)$$

For simplicity, we have used the total dpAGN fraction (f_{dp}) in place of non-binary dpAGN fraction, because 98% of the dpAGNs are due to mechanisms other than binary orbital motion (§ 5.1).

Combining the above two equations, we obtain:

$$f_{\text{Bin}} = f_{\text{dpBin}} + f_{\text{seBin}}/f_{\text{dp}} \simeq 100 f_{\text{seBin}} = 2.2^{+2.5}_{-0.8}\% \quad (3)$$

$$c_{\text{dp}} = f_{\text{dpBin}}/f_{\text{Bin}} \simeq f_{\text{dpBin}}/(100 f_{\text{seBin}}) = 1.0^{+1.6}_{-0.5}\% \quad (4)$$

Our nominal binary AGN fraction lies close to the upper limit of that of Shen et al. (2011a) (0.5 – 2.5%), but the double-peaked selection completeness is an order-of-magnitude lower. This implies that the characteristic relative velocity of binary AGNs is lower than the 500 km s^{-1} assumed by Shen et al. (2011a).

There is a non-negligible probability that SMBHs in a merging pair are accreting simultaneously by chance, appearing as a binary AGN. If interactions do not enhance nuclear accretion, we would expect $\lesssim 0.3\%$ of AGNs are kpc-scale binaries. This “chance” binary fraction is simply the product of the average AGN duty cycle ($\lesssim 1\%$ for $M_{\text{BH}} \gtrsim 3 \times 10^7 M_{\odot}$ at $z = 0.5$; Shankar et al. 2009) and the $\sim 29\%$ merger fraction of AGNs (assuming it is the same as that of the dpAGNs). We adopted the 1% duty cycle because the black hole masses of the type-1 dpAGNs are all greater than $3 \times 10^7 M_{\odot}$ with a

¹⁴ These are objects that are double-peaked because of gas kinematics instead of orbital motion.

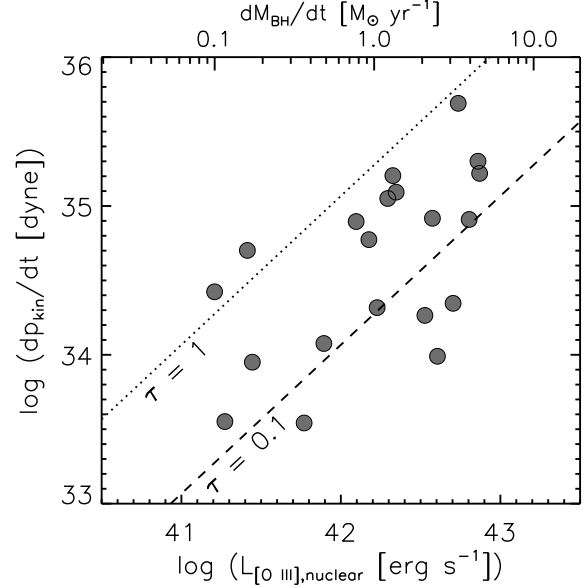


FIG. 6.— Momentum injection rate vs. nuclear [O III] luminosity ($2''$ -diameter aperture) for the 20 SNIFS-identified ENLRs (Fig. 4). The top axis shows the corresponding black hole accretion rates, calculated assuming $L_{\text{bol}} = 3500 L_{[\text{O III}]}$ (Heckman et al. 2004) and a radiative efficiency $\epsilon = 0.1$. The dotted and dashed lines indicate the momentum injection rates from radiation pressure of the current AGN luminosity at optical depths $\tau = 1.0$ and 0.1 , respectively.

mean value of $3 \times 10^8 M_{\odot}$ (Shen et al. 2011b). The observed binary fraction (f_{Bin}) is already five times higher than this “chance” binary fraction even at the lower bound of the 1σ confidence interval. This result provides evidence that galaxy interactions enhance AGN activities (i.e., increasing the AGN duty cycle from $\sim 1\%$ to $8^{+8}_{-3}\%$), although a larger sample of binary AGNs and a more sophisticated calculation incorporating AGN [O III] luminosity functions and merger rates (e.g., Yu et al. 2011) are needed to draw the final conclusion.

5.3. The Formation of Extended Narrow-Line Regions

Although inefficient for identifying binary AGNs, the double-peaked selection technique is efficient for identifying ENLRs around AGNs (§ 5.1): the SNIFS observations have accumulated 20 ENLRs at $z < 0.6$. Here we attempt to constrain the formation of such extended nebulae with the current data.

The mass of a fully ionized cloud is proportional to the luminosity of hydrogen recombination lines at a given electron density (n_e):

$$\begin{aligned} M_{\text{H}} &= m_p n_e V f \\ &= m_p L_{\text{H}\beta} / (\alpha_{\text{H}\beta} n_e h\nu) \\ &= 6.8 \times 10^7 M_{\odot} (L_{\text{H}\beta} / 10^{40} \text{ erg s}^{-1}) (1 \text{ cm}^{-3} / n_e) \end{aligned} \quad (5)$$

where V is the total volume occupied by the cloud, f is the filling factor, m_p is the proton mass, $\alpha_{\text{H}\beta}$ the case-B recombination coefficient of H β ($3.03 \times 10^{-14} \text{ cm}^3 \text{ s}^{-1}$; Osterbrock & Ferland 2006), and $h\nu$ the energy of an H β photon ($4.09 \times 10^{-12} \text{ erg}$). Adopting an average [O III] $\lambda 5007/\text{H}\beta$ ratio of 6 and $n_e = 1 \text{ cm}^{-3}$, the total masses in the ENLRs range from 8×10^7 to $2 \times 10^{10} M_{\odot}$. To avoid the “classical” NLR in the inner part, we integrated only the pixels at distances greater than $1''$ from the nuclei.

Further, we can estimate the total momentum ($p_{\text{kin}} = M_H v$) of the ionized gas with the velocity maps. Finally, the size of the ENLR (§ 5.4) divided by the maximum line-of-sight velocity gives a dynamical timescale ($t = R_{\text{NLR}}/v_{\text{max}}$) between 8 and 70 Myrs, consistent with the typical AGN lifetime. Assuming the momentum has been accumulated throughout the dynamical timescale, we can estimate the rate of momentum injection ($\dot{p}_{\text{kin}} \simeq p_{\text{kin}}/t$), a diagnostic that can be compared with models.

It is possible that the radiation pressure from the AGN created the ENLRs, because the gas is believed to be dusty (Dopita et al. 2002; Groves et al. 2004). Our sample is a mixture of type-1 and type-2 AGNs, so we used the nuclear [O III] $\lambda 5007$ luminosity to infer the AGN bolometric luminosity ($L_{\text{bol}} = 3500L_{[\text{O III}]}$; Zakamska et al. 2003; Heckman et al. 2004). The rate of momentum injection from radiation pressure is $\dot{p} = \tau L_{\text{bol}}/c$, where τ is the effective optical depth and c is the speed of light. Figure 6 compares the measured rate of momentum injection with the expected rate of injection from radiation pressure at the current AGN luminosity. It shows that radiation pressure is sufficient to drive the outflow if the ENLR is moderately optically thick to the AGN radiation.

The uncertainties in this analysis are dominated by the lack of knowledge on the mass-weighted electron density. We have adopted a density of 1 cm^{-3} because of the success of the two-phase photoionization model in fitting the emission lines of quasar EELRs (Stockton et al. 2002; Fu & Stockton 2007). There, we have also shown that [O II] or [S II] doublets overestimate mass-weighted electron densities because high-density low-excitation regions dominate [O II] and [S II] emission. Because the momentum is inversely proportional to the density, the data points in Fig. 6 easily can be offset by one dex along the vertical direction, compromising the conclusion. Detailed photoionization modeling on deeper spectra is needed to better constrain the formation of the ENLRs.

5.4. Size–Luminosity Relation of Narrow-Line Regions

AGN photoionized gas extending over kpc-scales has been detected around QSOs (Stockton & MacKenty 1987) and Seyfert galaxies (Unger et al. 1987; Mulchaey et al. 1996) for over three decades. Inspired by the size-luminosity relation of AGN broad-line regions (e.g., Wandel et al. 1999), several more recent studies have suggested a similar correlation for the NLRs (e.g., Bennert et al. 2002; Schmitt et al. 2003; Greene et al. 2011). Because of the importance of this relation to our understanding of the NLR, we re-examine this relation with the SNIFS data. Integral-field spectroscopy is well-suited for this kind of study because it combines the advantages of previous long-slit spectroscopy (better surface-brightness sensitivity) and *HST* narrow-band imaging (more complete spatial coverage).

We determined the NLR radius as the longest distance from the nucleus to any lenslet with valid [O III] $\lambda 5007$ detections, i.e., emission-line peak-to-noise ratios greater than 2.0. Figure 7 plots the NLR radius as a function of [O III] luminosity integrated over the entire SNIFS field of view. We measured the sizes of both ENLRs and unresolved NLRs. For the latter, the measurements are considered as upper limits.

We compare the best-fit relations from previous studies and our data. Because we reached a similar depth as the long-slit study of Greene et al. (2011), which is an order-of-magnitude deeper than those from *HST* narrow-band imaging

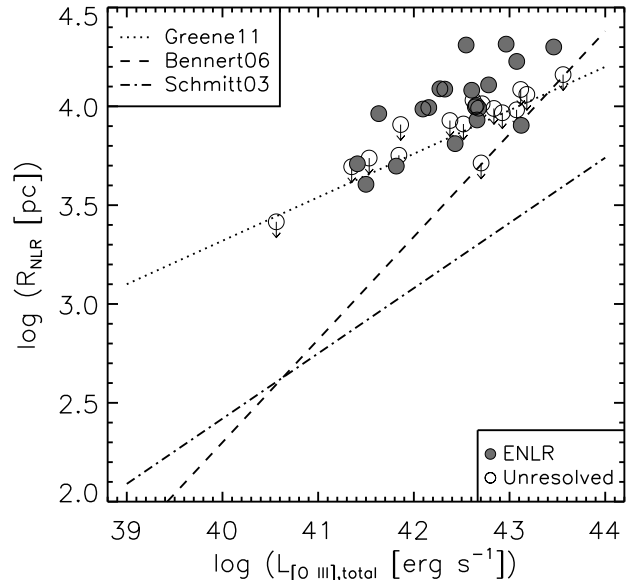


FIG. 7.— Size-luminosity relation of dpAGN NLRs. The data points are SNIFS-observed dpAGNs. Spatially resolved NLRs (or ENLRs) are filled circles, while unresolved NLRs are open circles with downward arrows. Binary AGNs have been excluded. The dotted, dashed, and dot-dashed lines show the size-luminosity relations from Greene et al. (2011), Bennert et al. (2002), and Schmitt et al. (2003), respectively.

($> 2 - 12 \times 10^{-15} \text{ erg s}^{-1} \text{ cm}^{-2} \text{ arcsec}^{-2}$; Bennert et al. 2002), our measurements are more consistent with the former than the latter. Considering the upper limits from the unresolved NLRs, the dispersion of this relation is at least 0.3 dex.

6. SUMMARY

We have used integral-field spectroscopy and $0.1''$ -resolution broad-band images to investigate the nature of double-peaked [O III] AGNs selected from the SDSS spectroscopic sample. Our main conclusions can be summarized as follows:

1. The relative velocity of a merging pair, each associated with an AGN NLR, accounts for only $\sim 2\%$ of the double-peaked [O III] AGNs. Gas kinematics produced $\sim 98\%$ of the double-peaked [O III] AGNs, which split almost evenly between spatially resolved and unresolved NLRs in seeing-limited data. We find the same fraction ($\sim 50\%$) of extended narrow-line regions around mergers and isolated dpAGNs.
2. We identified two binary AGNs from sources where gas kinematics produced the double-peaked [O III] lines. The relatively high fraction of such serendipitous binaries implies a low completeness ($\sim 1\%$) of double-peaked selection to binary AGNs and a total binary AGN fraction of $2.2^{+2.5}_{-0.8}\%$ in all SDSS AGNs at $z < 0.6$. The binary AGN fraction implies an AGN duty cycle ($8^{+8}_{-3}\%$) much higher than the average AGN duty cycle ($\lesssim 1\%$), suggesting galaxy interactions enhance nuclear accretion.
3. About 29% of the dpAGNs appear to be mergers at $0.1''$ -resolution. But multiple black holes are simultaneously accreting only in 15–42% of these mergers. The upper limit included the seven ambiguous cases.

Therefore, only 4–12% of double-peaked SDSS AGNs could be binary AGNs.

4. The total mass of the ionized gas in the 20 extended narrow-line regions in the SNIFS sample range from 8×10^7 to $2 \times 10^{10} M_{\odot}$, assuming an electron density of 1 cm^{-3} . We show that the radiation pressure from the AGN could have expelled enough gas to 10 kpc scales over the AGN lifetime and therefore created the extended narrow-line regions.
5. We measure a size-luminosity relation for the NLRs consistent with that of Greene et al. (2011) from ground-based long-slit spectra. There is at least 0.3 dex dispersion around the best-fit power-law.

Although this work was first motivated by the belief that the double-peaked AGN sample offers the best candidates to search for kpc-scale binary AGNs, we and others (Shen et al. 2011a; Rosario et al. 2011) have shown that this selection is primarily identifying AGNs with secondary peaks due to ionized gas kinematics. Furthermore, through this study we have realized that the double-peaked sample offers very little advantage over more general AGN samples in terms of searching for binary AGNs, because the binary fraction in all AGNs ($\sim 2.4\%$) is only slightly lower than that in dpAGNs ($\sim 4\%$). Finally, we caution that because the binary AGNs that we

found are either type-1–type-2 or type-2–type-2 pairs, we can not completely rule out the single AGN scenario: that the gas in one of the nuclei is photoionized by the AGN in the neighboring galaxy. The ultimate test awaits future high-resolution X-ray images from *Chandra* and/or radio images from the EVLA.

It is a pleasure to thank Steven Rodney, Nick Moskovitz, Mark Willman, and Eric Gaidos for advice on SNIFS observations, and Jessica Lu, Tucker Jones, Peter Capak, and Nick Scoville for helpful discussions. We thank the referee for cogent comments that helped improve the paper. ADM is a research fellow of the Alexander von Humboldt Foundation of Germany. AS was partially supported by NSF grant AST-0807900. SGD was partially supported by NSF grant AST-0909182 and the Ajax Foundation. GA was supported by the Director, Office of Science, Office of High Energy Physics, of the U.S. Department of Energy under Contract No. DE-AC02-05CH11231. The authors wish to recognize and acknowledge the very significant cultural role and reverence that the summit of Mauna Kea has always had within the indigenous Hawaiian community. We are most fortunate to have the opportunity to conduct observations from this mountain.

Facilities: UH:2.2m (SNIFS), Keck:II (LGSAO/NIRC2, LGSAO/OSIRIS), Sloan

REFERENCES

- Aldering, G., et al. 2002, in SPIE Conference Series, Vol. 4836, 61–72
 Aldering, G., et al. 2006, *ApJ*, 650, 510
 Bacon, R., et al. 1995, *A&AS*, 113, 347
 Baldwin, J. A., Phillips, M. M., & Terlevich, R. 1981, *PASP*, 93, 5
 Barnes, J. E., & Hernquist, L. 1996, *ApJ*, 471, 115
 Begelman, M. C., Blandford, R. D., & Rees, M. J. 1980, *Nature*, 287, 307
 Bennert, N., Falcke, H., Schulz, H., Wilson, A. S., & Wills, B. J. 2002, *ApJ*, 574, L105
 Bianchi, S., Chiaberge, M., Piconcelli, E., Guainazzi, M., & Matt, G. 2008, *MNRAS*, 386, 105
 Boroson, T. A., & Lauer, T. R. 2009, *Nature*, 458, 53
 Cameron, E. 2011, *Publications of the Astronomical Society of Australia*, 28, 128
 Cardelli, J. A., Clayton, G. C., & Mathis, J. S. 1989, *ApJ*, 345, 245
 Chen, K., Halpern, J. P., & Filippenko, A. V. 1989, *ApJ*, 339, 742
 Comerford, J. M., et al. 2009, *ApJ*, 698, 956
 Davies, R. I. 2007, *MNRAS*, 375, 1099
 Djorgovski, S. 1991, in *The space distribution of quasars*, Vol. 21, 349–353
 Djorgovski, S., Perley, R., Meylan, G., & McCarthy, P. 1987, *ApJ*, 321, L17
 Dopita, M. A., Groves, B. A., Sutherland, R. S., Binette, L., & Cecil, G. 2002, *ApJ*, 572, 753
 Dunkley, J., et al. 2009, *ApJS*, 180, 306
 Eracleous, M., Boroson, T. A., Halpern, J. P., & Liu, J. 2011, preprint, arXiv:1106.2952
 Eracleous, M., & Halpern, J. P. 2003, *ApJ*, 599, 886
 Eracleous, M., Halpern, J. P., Gilbert, A. M., Newman, J. A., & Filippenko, A. V. 1997, *ApJ*, 490, 216
 Fischer, T. C., Crenshaw, D. M., Kraemer, S. B., Schmitt, H. R., Mushotsky, R. F., & Dunn, J. P. 2011, *ApJ*, 727, 71
 Fu, H., Myers, A. D., Djorgovski, S. G., & Yan, L. 2011a, *ApJ*, 733, 103
 Fu, H., & Stockton, A. 2007, *ApJ*, 666, 794
 —. 2009a, *ApJ*, 690, 953
 —. 2009b, *ApJ*, 696, 1693
 Fu, H., et al. 2011b, *ApJ*, 740, L44
 Gaskell, C. M. 1983, in *Liege International Astrophysical Colloquia*, Vol. 24, 473–477
 Gaskell, C. M. 1996, *ApJ*, 464, L107
 Gelderman, R., & Whittle, M. 1994, *ApJS*, 91, 491
 Gerke, B. F., et al. 2007, *ApJ*, 660, L23
 Green, P. J., Myers, A. D., Barkhouse, W. A., Mulchaey, J. S., Bennert, V. N., Cox, T. J., & Aldcroft, T. L. 2010, *ApJ*, 710, 1578
 Greene, J. E., Zakamska, N. L., Ho, L. C., & Barth, A. J. 2011, *ApJ*, 732, 9
 Groves, B. A., Dopita, M. A., & Sutherland, R. S. 2004, *ApJS*, 153, 9
 Heckman, T. M., Kauffmann, G., Brinchmann, J., Charlot, S., Tremonti, C., & White, S. D. M. 2004, *ApJ*, 613, 109
 Hennawi, J. F., et al. 2006, *AJ*, 131, 1
- Junkkarinen, V., Shields, G. A., Beaver, E. A., Burbidge, E. M., Cohen, R. D., Hamann, F., & Lyons, R. W. 2001, *The Astrophysical Journal Letters*, 549, L155
 Kauffmann, G., et al. 2003, *MNRAS*, 346, 1055
 Kellermann, K. I., Sramek, R., Schmidt, M., Shaffer, D. B., & Green, R. 1989, *AJ*, 98, 1195
 Kewley, L. J., Groves, B., Kauffmann, G., & Heckman, T. 2006, *MNRAS*, 372, 961
 Kochanek, C. S., Falco, E. E., & Muñoz, J. A. 1999, *ApJ*, 510, 590
 Komossa, S., Burwitz, V., Hasinger, G., Predehl, P., Kaastra, J. S., & Ikebe, Y. 2003, *ApJ*, 582, L15
 Komossa, S., Zhou, H., & Lu, H. 2008, *ApJ*, 678, L81
 Kormendy, J., & Richstone, D. 1995, *ARA&A*, 33, 581
 Koss, M., et al. 2011, *ApJ*, 735, L42
 Krabbe, A., Gasaway, T., Song, I., Iserlohe, C., Weiss, J., Larkin, J. E., Barczys, M., & Lafreniere, D. 2004, in SPIE Conference Series, Vol. 5492, 1403–1410
 Lantz, B., et al. 2004, in SPIE Conference Series, Vol. 5249, 146–155
 Larkin, J., et al. 2006, in SPIE Conference Series, Vol. 6269, 42
 Liu, X., Greene, J. E., Shen, Y., & Strauss, M. A. 2010a, *ApJ*, 715, L30
 Liu, X., Shen, Y., Strauss, M. A., & Greene, J. E. 2010b, *ApJ*, 708, 427
 Liu, X., Shen, Y., Strauss, M. A., & Hao, L. 2011, preprint, arXiv:1104.0950
 Markwardt, C. B. 2009, in ASP Conference Series, *Astronomical Data Analysis Software and Systems XVIII*, D. A. Bohlender, D. Durand, and P. Dowler, eds., Vol. 411, 251
 McGurk, R. C., Max, C. E., Rosario, D. J., Shields, G. A., Smith, K. L., & Wright, S. A. 2011, *ApJ*, 738
 Mulchaey, J. S., Wilson, A. S., & Tsvetanov, Z. 1996, *ApJS*, 102, 309
 Myers, A. D., Brunner, R. J., Richards, G. T., Nichol, R. C., Schneider, D. P., & Bahcall, N. A. 2007, *ApJ*, 658, 99
 Myers, A. D., Richards, G. T., Brunner, R. J., Schneider, D. P., Strand, N. E., Hall, P. B., Blomquist, J. A., & York, D. G. 2008, *ApJ*, 678, 635
 Osterbrock, D. E., & Ferland, G. J. 2006, *Astrophysics of gaseous nebulae and active galactic nuclei* (Sausalito, CA: University Science Books, 2006)
 Richstone, D., et al. 1998, *Nature*, 395, 14
 Rodriguez, C., Taylor, G. B., Zavala, R. T., Peck, A. B., Pollack, L. K., & Romani, R. W. 2006, *ApJ*, 646, 49
 Rosario, D. J., McGurk, R. C., Max, C. E., Shields, G. A., & Smith, K. L. 2011, preprint, arXiv:1102.1733
 Rosario, D. J., Shields, G. A., Taylor, G. B., Salviander, S., & Smith, K. L. 2010, *ApJ*, 716, 131
 Schlegel, D. J., Finkbeiner, D. P., & Davis, M. 1998, *ApJ*, 500, 525
 Schmitt, H. R., Donley, J. L., Antonucci, R. R. J., Hutchings, J. B., Kinney, A. L., & Pringle, J. E. 2003, *ApJ*, 597, 768
 Shankar, F., Weinberg, D. H., & Miralda-Escudé, J. 2009, *ApJ*, 690, 20
 Shen, Y., Liu, X., Greene, J. E., & Strauss, M. A. 2011a, *ApJ*, 735, 48

TABLE 1
INTEGRAL-FIELD SPECTROSCOPY SAMPLE

SDSS Name	IFS	Exptime (second)	UT	Seeing (")	Depth	Image Source
(1)	(2)	(3)	(4)	(5)	(6)	(7)
012613.3+142013	SNIFS/B&R	900	100809	0.7	0.9	...
040001.6-065254	SNIFS/R	1800	100809	0.7	3.2	OSIRIS/Hbb
080315.7+483603*	SNIFS/B&R	900	110326	0.4	1.6	NIRC2/Kp
080841.2+481352	OSIRIS/Kn2	1800	100307	0.7	...	NIRC2/Kp
081507.4+430427*	SNIFS/B&R	1200	110329	0.7	3.8	NIRC2/Kp
090246.9+012028	SNIFS/B&R	1200	110329	0.7	1.8	NIRC2/Kp
091646.0+283527	SNIFS/B&R	1200	110329	0.6	4.1	NIRC2/Kp
092455.2+051052	SNIFS/B&R	3600	110329	0.7	2.8	NIRC2/Kp
094032.3+311329	SNIFS/B&R	1800	110329	1.1	1.8	NIRC2/Kp
095207.6+255257*	SNIFS/B&R	2400	110326	0.4	0.6	OSIRIS/Hbb
105052.5+083935	OSIRIS/Kn3	2400	100307	0.7	...	NIRC2/Kp
105104.5+625159*	SNIFS/B&R	1200	110326	0.5	1.0	NIRC2/Kp
110851.0+065901	SNIFS/B&R	1200	110329	0.8	2.1	NIRC2/Kp
114642.5+511030	SNIFS/B&R	1200	110326	0.4	1.5	NIRC2/Kp
115106.7+471158*	SNIFS/B&R	1200	110326	0.6	0.6	NIRC2/Kp
115523.7+150757*	SNIFS/B&R	900	101121	0.5	3.6	NIRC2/Kp
123915.4+531415*	SNIFS/B&R	1800	100804	0.5	1.2	NIRC2/Kp
124037.8+353437	OSIRIS/Kn3	1800	100307	0.7	...	OSIRIS/Hbb
124859.7-025731*	SNIFS/B&R	2400	110326	0.4	0.6	NIRC2/Kp
125327.5+254747*	SNIFS/B&R	3600	110329	0.7	0.6	NIRC2/Kp
130128.8-005804	SNIFS/B&R	600	100808	0.6	6.3	ACS/F550M
130724.1+460401*	SNIFS/B&R	1800	100808	0.5	0.5	NIRC2/Kp
133226.3+060627	SNIFS/B&R	2400	110326	0.5	3.4	NIRC2/Kp
135024.7+240251*	SNIFS/B&R	2400	110326	0.8	1.1	NIRC2/Kp
135646.1+102609	SNIFS/B&R	900	100804	0.7	8.2	NIRC2/Kp
140816.0+015528	SNIFS/B&R	3600	100809	0.5	1.2	...
144012.8+615633*	SNIFS/B&R	1200	110329	0.6	0.9	NIRC2/Kp
150243.1+111557*	SNIFS/B&R	1800	100804	0.8	1.3	NIRC2/Kp
150437.7+541150*	SNIFS/B&R	1200	110329	0.6	1.5	NIRC2/Kp
151656.6+183022	SNIFS/B&R	900	100809	0.6	0.9	...
151735.2+214533*	SNIFS/B&R	3600	100804	0.7	0.5	NIRC2/Kp
152431.4+323751	SNIFS/B&R	1800	100809	0.6	0.3	...
153231.8+420343*	SNIFS/B&R	1200	110329	0.7	1.0	NIRC2/Kp
154107.8+203609*	SNIFS/B&R	3600	100806	0.6	1.0	NIRC2/Kp
161826.9+081951*	SNIFS/B&R	900	100809	0.5	1.6	NIRC2/Kp
161847.9+215925*	SNIFS/B&R	1500	100809	0.6	0.8	NIRC2/Kp
164713.4+383140	SNIFS/B&R	1800	100809	0.6	1.0	...
165206.1+310708	SNIFS/B&R	1800	100806	0.6	2.3	NIRC2/Kp
171930.6+293413*	SNIFS/B&R	1200	110329	0.7	1.5	NIRC2/Kp
172049.2+310646	SNIFS/B&R	1500	100804	0.5	1.6	NIRC2/Kp
233313.2+004912	SNIFS/B&R	900	100808	0.5	2.2	NIRC2/Kp
235256.6+001155	SNIFS/B&R	900	100809	0.6	1.4	NIRC2/Kp

NOTE. — Column 1: J2000 designation. type-1s are indicated by stars. Column 2: Name of the Integral-Field Spectrograph (IFS). Column 3: Total exposure time of the spectrum. Column 4: UT date (yymmdd) of the spectrum. Column 5: Outside seeing at 5000Å during the spectroscopic observation (<http://kiloaolao.soest.hawaii.edu/current/seeing/>). Column 6: [O III] surface brightness depth of the reduced SNIFS datacube in 10^{-16} erg s $^{-1}$ cm $^{-2}$ arcsec $^{-2}$, see § 2.2.2. Column 7: Source of the high-resolution broad-band image.

Shen, Y., et al. 2011b, *ApJS*, 194, 45
Shields, G. A., Rosario, D. J., Junkkarinen, V., Chapman, S. C., Bonning, E. W., & Chiba, T. 2011, arXiv e-prints, 1109, 1524
Smith, K. L., Shields, G. A., Bonning, E. W., McMullen, C. C., Rosario, D. J., & Salviander, S. 2010, *ApJ*, 716, 866
Stockton, A., Canalizo, G., Fu, H., & Keel, W. 2007, *ApJ*, 659, 195
Stockton, A., Canalizo, G., Nelan, E. P., & Ridgway, S. E. 2004, *ApJ*, 600, 626
Stockton, A., & MacKenty, J. W. 1987, *ApJ*, 316, 584
Stockton, A., MacKenty, J. W., Hu, E. M., & Kim, T.-S. 2002, *ApJ*, 572, 735
Toomre, A., & Toomre, J. 1972, *ApJ*, 178, 623

Tsalmantza, P., Decarli, R., Dotti, M., & Hogg, D. W. 2011, arXiv e-prints, 1106, 1180
Unger, S. W., Pedlar, A., Axon, D. J., Whittle, M., Meurs, E. J. A., & Ward, M. J. 1987, *MNRAS*, 228, 671
Wandel, A., Peterson, B. M., & Malkan, M. A. 1999, *ApJ*, 526, 579
Wang, J.-M., Chen, Y.-M., Hu, C., Mao, W.-M., Zhang, S., & Bian, W.-H. 2009, *ApJ*, 705, L76
Wizinowich, P. L., et al. 2006, *PASP*, 118, 297
Xu, D., & Komossa, S. 2009, *ApJ*, 705, L20
Yu, Q., Lu, Y., Mohayaee, R., & Colin, J. 2011, arXiv e-prints, 1105, 1963
Zakamska, N. L., et al. 2003, *AJ*, 126, 2125

TABLE 2
 PROPERTIES OF DOUBLE-PEAKED [O III] AGNs WITH INTEGRAL-FIELD SPECTROSCOPY

SDSS Name	z	ΔV (km s ⁻¹)	$L_{[\text{O III}]}^b$ log(L_{\odot})	$L_{[\text{O III}]}^r$ log(L_{\odot})	FWHM ^b (km s ⁻¹)	FWHM ^r (km s ⁻¹)	R	$\Delta\theta$ ($''$)	ΔS (kpc)	Secondary Class	S11 Class
(1)	(2)	(3)	(4)	(5)	(6)	(7)	(8)	(9)	(10)	(11)	(12)
Orbital Motion											
095207.6+255257*	0.339	442	8.55	8.41	682	249	...	1.00	4.8
150243.1+111557*	0.390	657	9.84	8.96	384	354	36	1.39	7.4	ENLR	...
Extended Narrow-Line Region											
012613.3+142013	0.573	580	8.72	9.35	426	334	4698
040001.6-065254	0.171	391	8.43	8.73	344	397	10	NLR
081507.4+430427*	0.510	536	8.96	9.52	419	509	106	1.95	12.0
105104.5+625159*	0.436	364	9.25	8.19	847	167	1	1.52	8.6
110851.0+065901	0.182	204	8.74	8.27	686	159	28	0.73	2.2	ambiguous	binary
114642.5+511030	0.130	287	8.03	8.17	183	264	...	2.84	6.6	...	binary
115523.7+150757*	0.287	480	8.91	8.50	928	265	2	0.58	2.5	ambiguous	...
124037.8+353437	0.161	491	8.79	8.20	899	338	28	0.19	0.5	binary	...
124859.7-025731*	0.487	380	8.58	9.04	92	362	...	0.53	3.2	ambiguous	...
125327.5+254747*	0.483	688	8.74	8.25	1130	148	32	0.72	4.3	ambiguous	...
130724.1+460401*	0.352	518	8.30	8.32	629	208	...	2.37	11.7
133226.3+060627	0.207	409	7.79	8.04	271	439	...	1.58	5.4	...	binary
135646.1+102609	0.123	383	8.85	9.19	397	411	128	1.32	2.9	...	binary
140816.0+015528	0.166	339	7.64	7.67	167	216	11
150437.7+541150*	0.305	719	9.02	8.21	362	351
151735.2+214533*	0.399	324	8.62	8.06	781	124	...	1.10	5.9	ambiguous	...
161847.9+215925*	0.334	365	8.84	8.49	328	140	5
164713.4+383140	0.164	340	7.52	7.49	181	185
172049.2+310646	0.095	389	7.69	7.29	231	416	...	0.38	0.7	ambiguous	...
233313.2+004912	0.170	434	8.29	8.67	370	449	1234	ambiguous
235256.6+001155	0.167	322	7.98	7.86	287	212
Unresolved Narrow-Line Region											
080315.7+483603*	0.635	262	8.98	8.92	285	157	7	2.63	18.0
080841.2+481352	0.124	396	7.62	7.82	320	359
090246.9+012028	0.513	304	8.87	9.37	132	526	34	2.71	16.8
091646.0+283527	0.142	418	9.05	8.18	473	120	13	1.23	3.1
092455.2+051052	0.150	429	7.25	7.57	261	333	...	0.44	1.2	ambiguous	...
094032.3+311329	0.170	374	7.71	7.49	322	132	...	2.45	7.1
105052.5+083935	0.169	351	8.19	8.18	366	369
115106.7+471158*	0.318	644	9.20	9.33	774	667	3	1.29	6.0	binary	...
123915.4+531415*	0.202	715	7.87	7.76	297	825	75	1.26	4.2	ENLR	...
130128.8-005804	0.246	292	9.11	8.26	731	283	17	1.40	5.4
135024.7+240251*	0.557	277	8.69	8.57	190	227	...	1.80	11.6
144012.8+615633*	0.275	505	8.89	8.42	1494	298	2	ENLR	...
151656.6+183022	0.580	400	9.77	9.53	693	354	26314
152431.4+323751	0.629	480	9.41	8.92	378	307
153231.8+420343*	0.209	353	8.51	8.44	290	251
154107.8+203609*	0.508	441	8.96	8.63	374	241	...	2.00	12.3
161826.9+081951*	0.446	384	8.62	9.54	195	689	137
165206.1+310708	0.075	307	6.59	6.73	137	155	...	2.96	4.2
171930.6+293413*	0.180	1105	8.12	7.67	1265	776	2

NOTE. — Objects are grouped according to the origin of the double-peaked [O III] lines. Column 1: J2000 designation. type-1s are indicated by stars. Column 2: Redshift. Column 3: Velocity splitting between [O III] $\lambda 5007$ components: $\Delta V/c = [(1+z_r)^2/(1+z_b)^2 - 1]/[(1+z_r)^2/(1+z_b)^2 + 1]$, where z_r and z_b are the redshifts of the redshifted and blueshifted [O III] components, respectively. Columns 4 and 5: [O III] $\lambda 5007$ luminosity in log(L_{\odot}) for the blueshifted (b) and redshifted (r) line, corrected for Galactic extinction. Columns 6 and 7: [O III] $\lambda 5007$ FWHMs, corrected for the $\sigma = 65$ km s⁻¹ instrumental broadening. Column 8: Kellermann et al. (1989) radio loudness, $R = F_{\nu, 5\text{GHz}}/F_{\nu, 4400\text{\AA}}$. Columns 9 and 10: Projected angular separation (arcsec) and physical separation (kpc) between the main components in a merging system. Column 11: Secondary classification (§ 3). Column 12: Classification from Shen et al. (2011a).

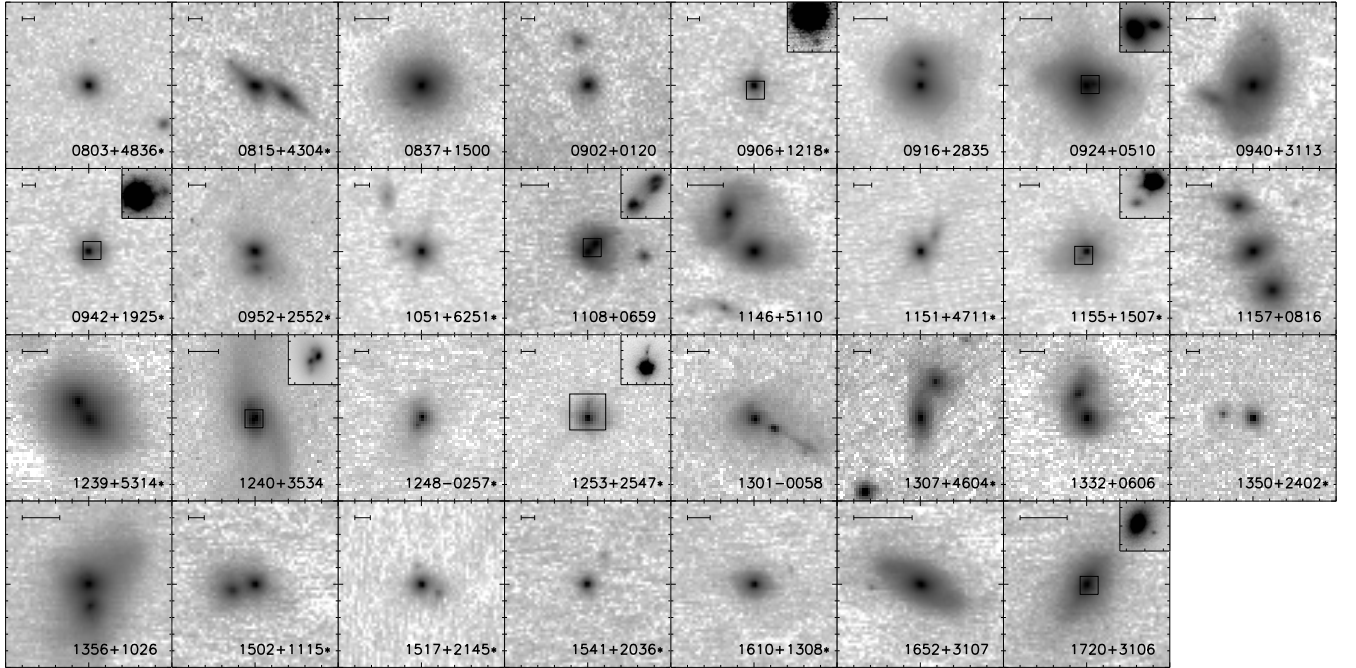


FIG. A1.— Keck II/LGSAO or *HST* images of dpAGNs that have companions within $3''$. Images are displayed in *asinh* (the inverse hyperbolic sine function) scales to bring up low surface brightness features. North is up and east is to the left ($10''$ stamps with $1''$ tickmarks). The scale bar indicates a transverse separation of 5 kpc. The insets show the components in linear scales for compact systems ($\Delta\theta < 1''$). The open boxes in the main panel delineate the regions covered by the insets. The tickmarks in the insets are spaced in $0.4''$.

APPENDIX

A. HIGH-RESOLUTION IMAGES OF DOUBLE-PEAKED AGNS

We show the high-resolution images of the 106 dpAGNs from our Keck LGSAO program and the *HST* archive in Figures A1 & A2 for objects with and without companions within $3''$, respectively. Tables A1 & A2 list the properties and observing details.

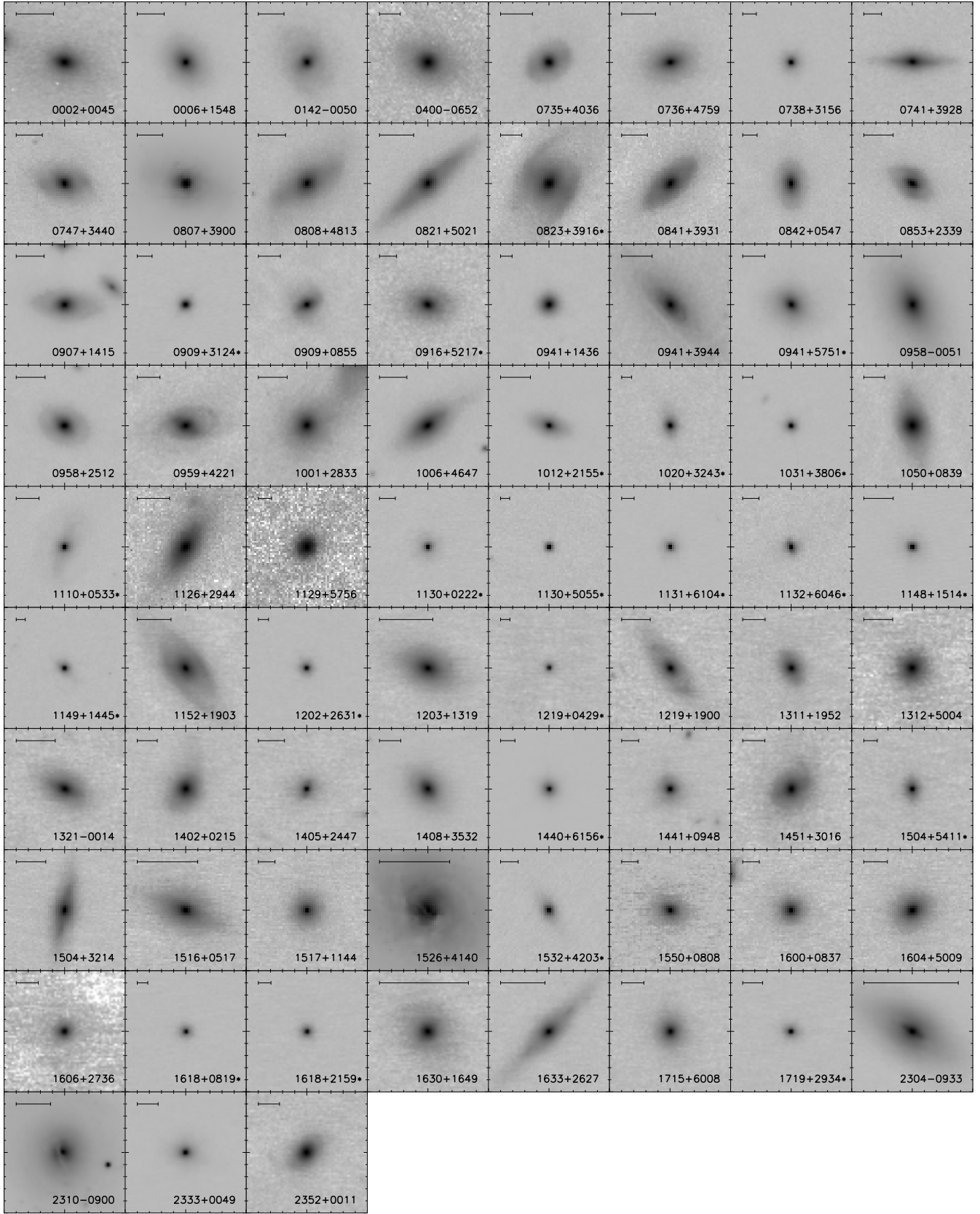


FIG. A2.— Same as Fig. A1, but for dpAGNs that do not have companions within $3''$. The scale bar indicates a transverse separation of 5 kpc except for SDSS J0807+3900 and SDSS J1526+4140, where it indicates 1 kpc.

TABLE A1
DOUBLE-PEAKED [O III] AGNS WITH COMPANIONS WITHIN 3''

SDSS Name	z	ΔV (km s^{-1})	R	$\Delta\theta$ ($''$)	ΔS (kpc)	Imager	Exptime (second)	UT	Seeing ($''$)	IFS	Ref
(1)	(2)	(3)	(4)	(5)	(6)	(7)	(8)	(9)	(10)	(11)	(12)
080315.7+483603*	0.635	262	7	2.63	18.0	NIRC2/Kp	420	110105	0.6	1	3
081507.4+430427*	0.510	536	106	1.95	12.0	NIRC2/Kp	540	110105	0.6	1	3
083713.5+150037	0.141	387	7	1.37	3.4	NIRC2/Kp	480	110106	0.9	0	1
090246.9+012028	0.513	304	34	2.71	16.8	NIRC2/Kp	600	110106	0.8	1	3
090615.9+121846*	0.644	357	...	0.61	4.2	NIRC2/Kp	448	110105	0.5	0	3
091646.0+283527	0.142	418	13	1.23	3.1	NIRC2/Kp	660	110106	1.0	1	1
092455.2+051052	0.150	429	...	0.44	1.2	NIRC2/Kp	660	110106	1.0	1	3
094032.3+311329	0.170	374	...	2.45	7.1	NIRC2/Kp	840	110106	1.0	1	1
094236.7+192541*	0.540	515	1	0.44	2.8	NIRC2/Kp	640	110105	0.5	0	3
095207.6+255257*	0.339	442	...	1.00	4.8	OSIRIS/Hbb	480	100306	0.7	1	3
105104.5+625159*	0.436	364	1	1.52	8.6	NIRC2/Kp	600	110105	0.5	1	3
110851.0+065901	0.182	204	28	0.73	2.2	NIRC2/Kp	192	100604	0.3	1	1
114642.5+511030	0.130	287	...	2.84	6.6	NIRC2/Kp	704	100604	0.4	1	1
115106.7+471158*	0.318	644	3	1.29	6.0	NIRC2/Kp	600	110105	0.4	1	3
115523.7+150757*	0.287	480	2	0.58	2.5	NIRC2/Kp	352	100603	0.7	1	3
115715.0+081632	0.201	375	...	2.61	8.6	NIRC2/Kp	448	100603	0.7	0	3
123915.4+531415*	0.202	715	75	1.26	4.2	NIRC2/Kp	1088	100604	0.3	1	3
124037.8+353437	0.161	491	28	0.19	0.5	OSIRIS/Hbb	960	100307	0.7	1	1
124859.7-025731*	0.487	380	...	0.53	3.2	NIRC2/Kp	768	100604	0.4	1	3
125327.5+254747*	0.483	688	32	0.72	4.3	NIRC2/Kp	420	110105	0.4	1	3
130128.8-005804	0.246	292	17	1.40	5.4	ACS/F550M	2148	030809	...	1	1
130724.1+460401*	0.352	518	...	2.37	11.7	NIRC2/Kp	448	100604	0.3	1	3
133226.3+060627	0.207	409	...	1.58	5.4	NIRC2/Kp	768	100604	0.4	1	1,3
135024.7+240251*	0.557	277	...	1.80	11.6	NIRC2/Kp	420	110105	0.4	1	3
135646.1+102609	0.123	383	128	1.32	2.9	NIRC2/Kp	704	100603	0.8	1	1
150243.1+111557*	0.390	657	36	1.39	7.4	NIRC2/Kp	448	100603	0.7	1	3
151735.2+214533*	0.399	324	...	1.10	5.9	NIRC2/Kp	960	100604	0.4	1	3
154107.8+203609*	0.508	441	...	2.00	12.3	NIRC2/Kp	448	100604	0.3	1	3
161027.4+130807*	0.229	326	...	2.35	8.6	NIRC2/Kp	192	100604	0.3	0	3
165206.1+310708	0.075	307	...	2.96	4.2	NIRC2/Kp	320	100603	0.6	1	1,2
172049.2+310646	0.095	389	...	0.38	0.7	NIRC2/Kp	384	100603	0.5	1	1

NOTE. — Observing log and properties of the 31 dpAGNs with close companions. Column 1: J2000 designation. type-1s are indicated by stars. Column 2: redshift. Column 3: velocity splitting between [O III] $\lambda 5007$ components. Column 4: Kellermann et al. (1989) radio loudness, $R = F_{\nu, 5\text{GHz}}/F_{\nu, 4400\text{\AA}}$. Columns 5,6: Projected angular separation (arcsec) and physical separation (kpc) between the main components in a merging system. Column 7: name of the imager and the filter. Column 8: total exposure time of the image. Column 9: UT date (yymmdd) of the image. Column 10: outside seeing at 5000Å during the imaging observation. Column 11: IFS data available? 1 - yes, 0 - no. Column 12: source references—(1) Liu et al. (2010b), (2) Wang et al. (2009), (3) Smith et al. (2010).

TABLE A2
DOUBLE-PEAKED [O III] AGNs WITHOUT COMPANIONS WITHIN 3''

SDSS Name	z	ΔV (km s^{-1})	R	Imager	Exptime (second)	UT	Seeing ($''$)	IFS	Ref
(1)	(2)	(3)	(4)	(5)	(6)	(7)	(8)	(9)	(10)
000249.1+004505	0.087	534	7	NIRC2/Kp	192	110105	0.6	0	1,2
000656.9+154848	0.125	382	...	NIRC2/Kp	300	110105	0.7	0	2
014209.0-005050	0.133	248	...	NIRC2/Kp	240	110105	0.7	0	2
040001.6-065254	0.171	391	10	OSIRIS/Hbb	240	100306	0.7	1	1
073509.5+403624	0.103	264	...	NIRC2/Kp	420	110105	0.7	0	2
073656.5+475947	0.096	257	21	NIRC2/Kp	240	110105	0.7	0	1
073849.8+315612	0.297	297	506	NIRC2/Kp	240	110105	0.7	0	1
074129.7+392836	0.210	429	28	NIRC2/Kp	240	110105	0.6	0	3
074729.8+344018	0.130	319	...	NIRC2/Kp	240	110105	0.6	0	2
080741.0+390015	0.023	637	2	WFPC2/F606W	500	950226	...	0	2
080841.2+481352	0.124	396	...	NIRC2/Kp	720	110106	0.6	1	1,2,3
082107.9+502116	0.095	338	6	NIRC2/Kp	360	110106	0.9	0	1,2
082357.8+391631*	0.166	580	...	NIRC2/Kp	420	110105	0.5	0	3
084130.2+393119	0.132	332	...	NIRC2/Kp	480	110106	1.0	0	1
084227.5+054716	0.275	490	404	NIRC2/Kp	480	110106	0.8	0	1
085358.6+233911	0.113	215	...	NIRC2/Kp	480	110106	0.9	0	1
090754.0+141509	0.120	285	...	NIRC2/Kp	900	110106	0.8	0	1
090947.9+312444*	0.264	977	2	NIRC2/Kp	420	110105	0.5	0	3
090958.3+085542	0.159	341	17	NIRC2/Kp	720	110106	0.9	0	3
091654.1+521723*	0.219	349	...	NIRC2/Kp	448	110105	0.5	0	3
094100.8+143614	0.383	854	59	NIRC2/Kp	480	110106	1.2	0	3
094124.0+394442	0.108	285	2814	WFPC2/F555W	600	990426	...	0	2
094144.8+575124*	0.159	339	322	NIRC2/Kp	420	110105	0.5	0	3
095833.2-005119	0.086	407	3	NIRC2/Kp	480	110106	1.2	0	1,2
095834.0+251235	0.116	336	4	NIRC2/Kp	480	110106	0.9	0	1
095920.5+422142	0.153	292	...	NIRC2/Kp	480	110106	0.8	0	1
100145.3+283330	0.116	513	...	NIRC2/Kp	360	110106	0.8	0	3
100654.2+464717	0.123	303	4	NIRC2/Kp	480	110106	0.8	0	1
101241.2+215556*	0.111	257	...	NIRC2/Kp	420	110105	0.5	0	3
102004.4+324343*	0.484	381	...	NIRC2/Kp	420	110105	0.5	0	3
103138.7+380652*	0.492	734	...	NIRC2/Kp	600	110105	0.5	0	3
105052.5+083935	0.169	351	...	NIRC2/Kp	480	110106	0.9	1	1
111013.2+053339*	0.152	755	...	NIRC2/Kp	600	110105	0.4	0	3
112659.5+294443	0.102	319	...	NIRC2/Kp	...	110106	0.9	0	1,2
112907.1+575605	0.313	314	36	NIRC2/Kp	540	110106	0.9	0	1
113021.0+022212*	0.241	402	...	NIRC2/Kp	640	110105	0.4	0	3
113045.3+505509*	0.592	252	...	NIRC2/Kp	420	110105	0.4	0	3
113105.1+610405*	0.338	427	...	NIRC2/Kp	600	110105	0.4	0	3
113257.8+604654*	0.233	353	...	NIRC2/Kp	420	110105	0.3	0	3
114852.7+151416*	0.113	306	...	NIRC2/Kp	420	110105	0.4	0	3
114908.5+144547*	0.595	208	...	NIRC2/Kp	420	110105	0.4	0	3
115249.3+190300	0.097	323	9	NIRC2/Kp	448	100603	0.6	0	1,2
120240.7+263139*	0.476	466	66	NIRC2/Kp	192	100604	0.4	0	3
120320.7+131931	0.058	292	156	NIRC2/Kp	224	100603	0.6	0	2
121911.2+042906*	0.555	459	...	NIRC2/Kp	64	100603	0.7	0	3
121957.5+190003	0.117	390	...	NIRC2/Kp	448	100603	0.6	0	1
131106.7+195234	0.156	314	...	NIRC2/Kp	448	100603	0.7	0	1
131236.0+500416	0.116	353	16	NIRC2/Kp	128	100604	0.4	0	2
132104.6-001446	0.082	330	...	NIRC2/Kp	448	100603	0.7	0	1
140231.6+021546	0.180	276	2553	NIRC2/Kp	448	100603	0.7	0	1
140534.8+244735	0.130	218	3	NIRC2/Kp	224	100604	0.4	0	1
140845.7+353218	0.166	371	16	NIRC2/Kp	448	100603	0.7	0	1
144012.8+615633*	0.275	505	2	NIRC2/Kp	320	100603	0.7	1	3
144157.2+094859	0.220	826	61	NIRC2/Kp	320	100604	0.4	0	3
145156.8+301603	0.158	512	...	NIRC2/Kp	320	100603	0.8	0	1
150437.7+541150*	0.305	719	...	NIRC2/Kp	256	100603	0.7	1	3
150452.3+321415	0.113	250	7	NIRC2/Kp	384	100603	0.8	0	2
151659.2+051752	0.051	326	8	NIRC2/Kp	160	100604	0.5	0	1,2
151757.4+114453	0.227	433	...	NIRC2/Kp	320	100603	0.7	0	3
152606.2+414014	0.008	281	30	WFPC2/F606W	500	940828	...	0	2
153231.8+420343*	0.209	353	...	NIRC2/Kp	448	100604	0.4	1	3
155009.6+080839	0.232	400	23	NIRC2/Kp	128	100604	0.3	0	1
160027.8+083743	0.227	422	3765	NIRC2/Kp	320	100604	0.3	0	1
160436.2+500958	0.146	366	...	NIRC2/Kp	320	100604	0.3	0	1,2
160631.4+273643	0.158	319	9	NIRC2/Kp	128	100604	0.4	0	1
161826.9+081951*	0.446	384	137	NIRC2/Kp	160	100603	0.6	1	3
161847.9+215925*	0.334	365	5	NIRC2/Kp	160	100603	0.6	1	3
163056.8+164957	0.034	301	2	NIRC2/Kp	192	100604	0.5	0	1
163316.0+262716	0.071	307	...	NIRC2/Kp	320	100603	0.6	0	2
171544.0+600835	0.157	348	62	NIRC2/Kp	320	100603	0.6	0	1,3
171930.6+293413*	0.180	1105	2	NIRC2/Kp	224	100603	0.6	1	3
230442.8-093345	0.032	320	8	NIRC2/Kp	320	100603	0.7	0	1,2
231052.0-090012	0.094	329	138	ACS/F606W	720	050819	...	0	1,2

TABLE A2 — *Continued*

SDSS Name	z	ΔV (km s^{-1})	R	Imager	Exptime (second)	UT	Seeing ($''$)	IFS	Ref
(1)	(2)	(3)	(4)	(5)	(6)	(7)	(8)	(9)	(10)
233313.2+004912	0.170	434	1234	NIRC2/Kp	384	100603	0.7	1	1
235256.6+001155	0.167	322	...	NIRC2/Kp	384	100604	0.5	1	1

NOTE. — Observing log and properties of the 75 dpAGNs without close companions in *HST* or Keck/LGSAO images. Column 1: J2000 designation. type-1s are indicated by stars. Column 2: redshift. Column 3: velocity splitting between [O III] $\lambda 5007$ components. Column 4: Kellermann et al. (1989) radio loudness, $R = F_{\nu, 5\text{GHz}}/F_{\nu, 4400\text{\AA}}$. Column 5: name of the imager and the filter. Column 6: total exposure time of the image. Column 7: UT date (yymmdd) of the image. Column 8: outside seeing at 5000Å during the imaging observation. Column 9: IFS data available? 1 - yes, 0 - no. Column 10: source references—(1) Liu et al. (2010b), (2) Wang et al. (2009), (3) Smith et al. (2010).